AFRL-RZ-WP-TP-2008-2112

DESIGN STRATEGIES TO MITIGATE UNSTEADY FORCING (PREPRINT)

John P. Clark

Turbine Branch
Turbine Engine Division

APRIL 2008

STINFO COPY

AIR FORCE RESEARCH LABORATORY
PROPULSION DIRECTORATE
WRIGHT-PATTERSON AIR FORCE BASE, OH 45433-7251
AIR FORCE MATERIEL COMMAND
UNITED STATES AIR FORCE

REPORT DOCUMENTATION PAGE

The public reporting burden for this collection of information is estimated to average 1 hour per response, including the time for reviewing instructions, searching existing data sources, searching existing data sources, gathering and maintaining the data needed, and completing and reviewing the collection of information. Send comments regarding this burden estimate or any other aspect of this collection of information, including suggestions for reducing this burden, to Department of Defense, Washington Headquarters Services, Directorate for Information Operations and Reports (0704-0188), 1215 Jefferson Davis Highway, Suite 1204, Arlington, VA 22202-4302. Respondents should be aware that notwithstanding any other provision of law, no person shall be subject to any penalty for failing to comply with a collection of information if it does not display a currently valid OMB control number. **PLEASE DO NOT RETURN YOUR FORM TO THE ABOVE ADDRESS**.

1. REPORT DATE (DD-MM-YY)	2. REPORT TYPE	3. DATES COVERED (From - To)
April 2008	Conference Paper Preprint	01 October 2007 – 24 April 2008

4. TITLE AND SUBTITLE	5a. CONTRACT NUMBER
DESIGN STRATEGIES TO MITIGATE UNSTEADY FORCING (PREPRINT)	In-house
	5b. GRANT NUMBER
	5c. PROGRAM ELEMENT NUMBER 62203F

6. AUTHOR(S)	5d. PROJECT NUMBER
John P. Clark	3066
	5e. TASK NUMBER 06
	5f. WORK UNIT NUMBER 306606W8

7. PERFORMING ORGANIZATION NAME(S) AND ADDRESS(ES)	8. PERFORMING ORGANIZATION REPORT NUMBER
Turbine Branch (AFRL/RZTT) Turbine Engine Division Air Force Research Laboratory, Propulsion Directorate Wright-Patterson Air Force Base, OH 45433-7251 Air Force Materiel Command, United States Air Force	AFRL-RZ-WP-TP-2008-2112

9. SPONSORING/MONITORING AGENCY NAME(S) AND ADDRESS(ES)		10. SPONSORING/MONITORING AGENCY ACRONYM(S)
Air Force Research Laboratory Propulsion Directorate Wright-Patterson Air Force Base, OH 45433-7251 Air Force Materiel Command United States Air Force	AFOSR/NA 875 North Randolph Street Suite 325, Room 3112 Arlington, VA 22203-1768	AFRL/RZTT
		11. SPONSORING/MONITORING AGENCY REPORT NUMBER(S) AFRL-RZ-WP-TP-2008-2112

12. DISTRIBUTION/AVAILABILITY STATEMENT

Approved for public release; distribution unlimited.

13. SUPPLEMENTARY NOTES

Conference paper submitted to the von Karman Institute for Fluid Dynamics Lecture Series 2008. Technical paper contains color. PAO Case Number: WPAFB 08-2965, 17 Apr 2008.

14. ABSTRACT

The ability to predict accurately the levels of unsteady forcing on turbine blades is critical to avoid high-cycle fatigue failures. Further, a demonstrated ability to make accurate predictions leads to the possibility of controlling levels of unsteadiness through aerodynamic design. Several ingredients were essential to the success achieved in this study. First, judicious post-processing of CFD solutions was required to ensure that proper periodicity was achieved, and this was contingent upon an understanding of basic concepts in digital signal processing that are essential to the accurate calculation of unsteady forces on airfoils. Second, time-resolved predictions were subjected to a thorough and rigorous validation study for the physics observed in the turbine of interest in a relevant environment. Third, a clear understanding of the necessary steps to obtain the most accurate solution possible given the fidelity of the predictive system employed was required, and this followed naturally from knowledge gained in the validation study. Finally, it was pertinent to ensure that design changes to reduce forcing did not result in new sources of high unsteady loading.

(second Abstract version appears on reverse side) →

15. SUBJECT TERMS

Turbomachinery, turbines, unsteady aerodynamics, resonant stresses, forced response

16. SECURITY CLASSIFICATION OF:			17. LIMITATION OF ABSTRACT:	18. NUMBER OF PAGES	19a. NAME OF RESPONSIBLE PERSON (Monitor)
a. REPORT Unclassified	**b. ABSTRACT** Unclassified	**c. THIS PAGE** Unclassified	SAR	60	John P. Clark
					19b. TELEPHONE NUMBER (Include Area Code) N/A

i

14. ABSTRACT (second version)

The ability to predict accurately the levels of unsteady forcing on turbine blades is critical to avoid high-cycle fatigue failures. Further, a demonstrated ability to make accurate predictions leads to the possibility of controlling levels of unsteadiness through aerodynamic design. This lecture presents a successful example of forcing-function prediction and control during the design cycle of a modern gas-turbine engine. 3D time-resolved computational fluid dynamics was used within the design cycle to predict accurately the levels of unsteady forcing on a single-stage high-pressure turbine blade. Then, nozzle-guide-vane geometry changes including asymmetric circumferential spacing and suction-side modification were considered and rigorously analyzed to reduce levels of unsteady pressures on the blade. Both means of forcing reduction were ultimately implemented in development engines, and these were shown successfully to reduce resonant stresses on the blade to levels in keeping with design intent. Several ingredients were essential to the success achieved in this study. First, judicious post-processing of the solutions was required to ensure that proper periodicity was achieved, and this was contingent upon an understanding of basic concepts in digital signal processing that are essential to the accurate calculation of unsteady forces on airfoils. Second, the time-resolved predictions were subjected to a thorough and rigorous validation study for the physics observed in the turbine of interest in a relevant environment. Third, a clear understanding of the necessary steps to obtain the most accurate solution possible given the fidelity of the predictive system employed was required, and this followed naturally from knowledge gained in the validation study. Finally, it was pertinent to ensure that there were no changes in unsteadiness that were potentially detrimental to vibratory modes not considered problematic previously.

Acknowledgments

1. Introduction

Periodic unsteadiness is inherent to flows in gas turbine engines, and in consequence very many studies have been devoted to the understanding of unsteady flows in turbomachines over a large number of years. There are seminal investigations that have delved into the theoretical (e.g. Tyler and Sofrin [1] and Rangwalla and Rai [2]), experimental (e.g. Dring et al. [3], Dunn and Haldeman [4]), and computational (e.g. Rai [5], Giles [6]) aspects of rotor-stator interactions. In addition, reviews of the state of the art are available (Greitzer et al. [7] and Sharma et al. [8]) as well as more general introductions to the subject (e.g. Paniagua and Denos [9]). In recent reviews of turbine durability and aerodynamic predictive tools, respectively, Dunn [10] and Adamczyk [11] have made the point that the fidelity of flowfield predictions has increased accordingly as the state-of-the-art for CFD calculations in the gas turbine industry has progressed. The increased predictive capability of turbine design codes has allowed for better turbomachinery designs and improved understanding of the physical mechanisms that are prevalent in turbomachines, especially when used to compliment experimental findings.

Greitzer et al. [7] discussed time-varying flowfields and the aero-mechanical excitation that can result from such unsteadiness. The authors stated that, in general, levels of unsteady forcing that give rise to High-Cycle Fatigue (HCF) problems during engine development had to that time not been well predicted. They described the current design process for turbine blades as one of resonant-avoidance. Modern structural-analysis tools are used to predict the natural frequencies of vibratory modes with acceptable accuracy, and these are plotted versus wheel speed on a Campbell diagram along with the frequencies of expected stress drivers in the system. Fig. 1.1 is one such diagram for the stainless-steel high turbine blade tested in the code validation study described in Section 3, below. A typical design practice might encompass ensuring that there are no expected resonances for any of the lower-order modes in the operating range of the machine (a turbine rig in the case of Fig. 1.1). However, sometimes this design practice is not feasible. So, Greitzer et al. [7] concluded that blade forced-response and the high-cycle fatigue failures that can result from it were of sufficient interest to the gas-turbine community that "…a decrease in the level of empiricism [in that area] would be of significant value in the engine development process." Practically, this meant that faster and more accurate predictions of the magnitudes of unsteady forcing functions were required.

Toward that end, developments in predictive methods such as multi-grid techniques and implicit dual time-stepping, coupled with parallelization of codes (Ni [12]) have made it possible for designers to execute 3-D, unsteady Navier-Stokes analyses routinely during the design cycle. So, designers can now routinely predict periodic-unsteady forcing functions and the calculation of resonant stresses in multi-row turbomachinery is now widespread in the industry [13-19]. Consequently, it is now possible to make design changes as necessary based on the outcome of such calcutions. Also, short-duration experimental facilities that allow for accurate modeling of modern gas-turbine flowfields (e.g. Jones et al. [20] and Dunn et al. [21]) are often used to assess the capabilities of state-of-the-art codes. In particular, the abilities of the codes to predict both the time-averaged and time-resolved pressure loadings on transonic airfoils were investigated (e.g. Rao et al. [22], Busby et al. [23], Hilditch et al. [24], and many others [25-28]). This has even been extended to include an assessment of the structural response due to forcing by Kielb et al. [29] and Hennings and Elliot [30] as well as both the aerodynamic and mechanical damping Kielb and Abhari [31]. In addition, design-optimization systems have been used effectively in conjunction with steady-state flow solvers

to reduce the strength of shock waves emanating from transonic turbine blades and decrease interaction losses as well as, presumably, resonant stresses by Jennions and Adamczyk [32].
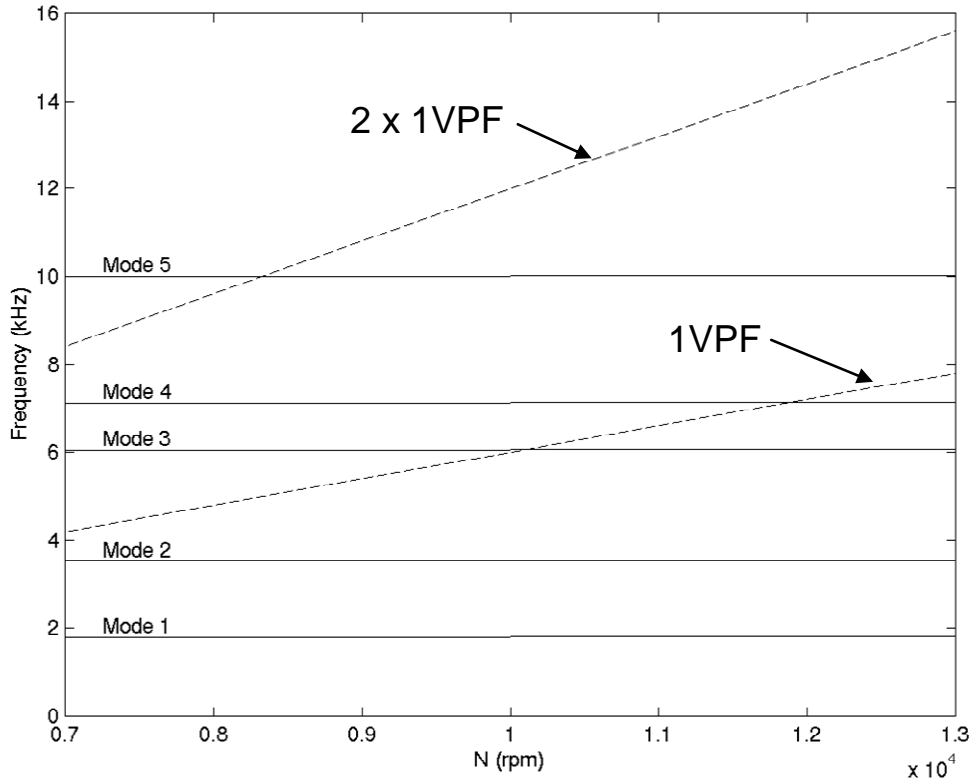

Fig. 1.1   Campbell diagram for a turbine blade tested in a short-duration rig

Turbomachinery designers often employ both steady-state and time-resolved predictive tools during the development of new engines. The major difference between the methods is the numerical treatment of the inter-row boundary. For steady-state turbomachinery simulations, common methodologies include the average-passage formulation of Adamczyk [11] and the mixing plane as employed in the Ni code [12, 33-35]. In the latter, the flow from an upstream blade row is circumferentially averaged and then the flow properties are passed into the downstream row as a radial profile. For many situations the difference between the steady-state flowfield and the time-average of an unsteady solution is minor. However, it is the time-resolved information that is often of most critical importance to the designer, as in the case of predicting resonant stresses in the machine.

Resonant stresses can arise as a consequence of the interaction between a turbine blade and airfoil wakes, potential fields, and/or shocks that can travel downstream and/or upstream through the engine. Turbine airfoil surfaces constantly encounter fluctuating flowfields induced by such flow structures. These can manifest as pressure fluctuations that impart time-varying forces that generate cyclic rotor vibratory stresses that can in turn reduce the life of the airfoil. Design methodologies are constantly being improved to predict these airfoil vibratory stresses, and such computations are now performed in the design cycle at many companies [13-19, and 36]. Additionally, design strategies to increase aerodynamic performance and turbine durability can have a detrimental effect on the fatigue life of turbine components. One performance-enhancing design feature involves the intentional shifting of

circumferential position between successive blade and/or vane rows [37-40]. Known as airfoil clocking, this relative difference in circumferential position is used to control the location of upstream airfoil wakes as they propagate through downstream airfoil passages in order to achieve a performance benefit in terms of increased efficiency. However, it is possible that the relative phase of an upstream-propagating potential field and downstream-propagating vortical disturbances could act to increase the unsteady load on a turbine blade that is located between clocked vane rows. In terms of turbine durability enhancements, sometimes fuel nozzles and turbine nozzle guide vanes are also clocked in an effort to reduce the heat load to downstream components [41-44]. Although there is no effect on the potential field inside the vane row [45], there is usually a variation in the unsteady pressure load on the turbine blades downstream of the vane.

2. Assessment of Periodic-Flow Convergence and Considerations from Digital Signal Processing

Predictions of time-resolved flowfields are now commonplace within the gas-turbine industry, and the results of such simulations are now being used to make design decisions during the development of new products. Hence, it is necessary for analysts to have a robust method to determine the level of convergence in design predictions. In this section, a method to determine the level of convergence in a predicted flowfield that is characterized by periodic-unsteadiness is presented. The method relies on fundamental concepts from digital signal processing that are themselves of great utility to the turbine engineer that is designing with unsteady aerodynamics in mind. These concepts include the discrete Fourier transform, cross-correlation, and Parseval's theorem. Often in predictions of vane-blade interaction in turbomachines, the period of the unsteady fluctuations is expected. In this method, the development of time-mean quantities, Fourier components (both magnitude and phase), cross-correlations, and integrated signal power are tracked at locations of interest from one period to the next as the solution progresses. Each of these separate quantities yields some relative measure of convergence that is subsequently processed to form a fuzzy set. Thus the overall level of convergence in the solution is given by the intersection of these sets. Examples of the application of this technique to predictions of vane/blade interaction using two separate solvers are given. It is shown that the method yields a robust determination of convergence. Also, the results of the technique can guide further analysis and/or post-processing of the flowfield. Finally, the method is useful for the detection of inherent unsteadiness in the flow, and so it can be used to prevent instances of non-synchronous vibration (NSV).

2.1 The Need for Rigorous Assessment of Periodic-Convergence

There are well established means for determining the accuracy of CFD simulations with respect to grid- and time-step convergence [46, 47]. This has led to policy statements from the engineering societies with respect to code verification and validation in general [48] and numerical accuracy in particular [49]. Of interest here is "iterative convergence." The policy statement from the ASME *Journal of Fluids Engineering* [49] states that, "stopping criteria for iterative calculations must be precisely explained, [and] estimates must be given for the corresponding convergence error." Iterative convergence criteria for steady-state simulations are well established: convergence is typically measured by tracking the iteration-to-iteration change of one or more flowfield quantities and looking for this value either to drop below a minimum threshold or to reach a zero slope. In an unsteady CFD simulation, the time-periodic nature of the flowfield precludes such a measure of convergence so some other technique is required.

In the gas-turbine industry designers often make simple qualitative judgments as to periodicity of the flow, and this is seldom based on interrogation of more than a few signals. Further, in most publications, discussion of unsteady convergence is cursory. One exception is due to Laumert et al. [50], who defined convergence of their unsteady simulation as occurring when the maximum deviation in static pressure between two periodic intervals was less than 0.1% over the airfoil surface at midspan. More recently, Ahmed and Barber [51] defined unsteady convergence in terms of time-varying Fast Fourier Transform (FFT) magnitudes calculated as the solution progresses. As time-resolved flowfield predictions become an ever increasing part of physics-based design systems the need for quantitative

measures of iterative convergence becomes critical. This is particularly true when time-resolved CFD is used during detailed design where both rapid turn-around time and predictive accuracy are critical.

Design-optimization systems are becoming more and more prevalent within the industry [52-54], and using time-accurate CFD within such a system necessarily requires quantitative convergence monitoring. The computational time required to obtain a valid solution when considering the currently-perturbed design parameter is critical to the feasibility of an optimization study. Without a converged solution from which to extract one or more parameters used in an objective (or fitness) function, it is not possible to determine a correct relationship between the perturbed design parameters and the design objective. One is left with little choice but to set each optimization perturbation to run a high number of iterations to ensure convergence. Consequently, the potential savings in the wall-clock time required to achieve a given objective is significant if a time-resolved convergence criterion is available.

A robust, quantitative process for assessing the level of convergence of a time-accurate simulation is required. Ideally, the method should consist of calculations that both track the progress of the simulation and allow for the detection of inherent unsteadiness in the flowfield. Here a measure of time-periodic convergence is defined and applied to a pair of unsteady simulations relevant to modern gas-turbine design. Again, application of the technique ensures the effective usage of time-accurate analyses during traditional design exercises to predict unsteady forcing, and it enables effective unsteady optimization.

2.2   Qualities of an Unsteady Convergence Criterion

Often in flowfield predictions in turbomachines, the period of the most significant unsteady fluctuations is expected from the circumferential interval modeled and the known wheel speed. During the execution of the time-accurate simulation, various aspects of the flowfield can be monitored at discrete intervals equal to some multiple of the computational time step. One can then calculate time-mean and time-resolved quantities of interest, and these may include but are not limited to the mass flow rates through domain inlet and exit boundaries, total pressures and temperatures (to obtain aero-performance), and static pressures on airfoil surfaces (to calculate resonant stresses). The collection of these quantities over the iteration history of the solution provides a set of discrete, time-varying signals which can be processed using standard signal processing techniques. Here, a set of signal processing operations, described in more detail by Ifeachor and Jervis [55] and in [56], were selected carefully for their relevance to both the design process in general and the case of periodic unsteadiness in particular.

As mentioned above, designers primarily perform unsteady simulations either to determine the effect of design changes on the time-mean characteristics of the machine (e.g. aero-performance or heat load) or to estimate resonant stresses on the airfoils. So, the development of both time-mean and time-resolved quantities is important for unsteady convergence monitoring. It is straightforward to track the former over periodic intervals, but the latter requires some consideration. Resonant stress analyses are typically performed at discrete engine orders consistent with the Campbell diagram of the airfoil row. Such calculations require accurate information on the unsteady forces on the airfoil row implying both magnitude and phase information at the frequencies of interest. These frequencies are driven by the airfoil counts in the machine where both the fundamental frequencies and a number of

5

harmonics may be important. So, it is necessary at a minimum to track the development of the magnitude and phase of relevant frequencies from periodic interval to periodic interval as well as time-mean quantities. Further, Jocker and Fransson [57] have clearly demonstrated the importance of the phase of periodic fluctuations in determining the level of excitation of a vibrating airfoil.

An effective convergence criterion for unsteady flows also allows for the possibility of inherent unsteadiness existing in a flowfield. This often occurs in turbomachinery as a consequence of vortex shedding at the trailing edge of the airfoil. Such shedding can occur whether or not a significant separation zone exists on the airfoil suction surface, and the frequency is dictated by the relevant Strouhal number of the flow over the airfoil. Fortunately, two other signal analysis measures, cross-correlation and the power spectral density, are useful under such circumstances.

One can cross-correlate a time-varying signal determined over one expected periodic interval with the same signal calculated over the next period. The result is itself a repeating signal that should have the same period as that expected in the simulation. Further, the magnitude of the cross-correlation coefficient at zero lag is a direct measure of how alike the signal is over each of the pair of expected periodic intervals. If significant inherent unsteadiness exists in the flowfield, then the magnitude at zero lag can be significantly less than one, and the period of the cross-correlation coefficient can occur at a number of lags that is inconsistent with that expected in the simulation.

In signal processing Parseval's theorem states that the integral of the power spectral density over a defined range of frequencies is equal to the contribution of fluctuations on that interval to the overall mean square of the signal. Consequently, one can sum the power spectral densities over all significant frequencies expected in the simulation and compare that to the overall mean square. If the summed signal power is not a large fraction of the overall signal variance, then either inherent unsteadiness exists in the flowfield or a higher harmonic of the fundamental passing frequencies is more significant than expected. Of course, it is also possible to use the level of the power spectral density to determine the frequencies associated with the inherent unsteadiness and/or the higher harmonics, and one can then alter the execution of the unsteady simulation (and subsequent post-processing and resonant stress analysis) accordingly.

It is clear that all of the above measures are important for an assessment of unsteady convergence, and a means for combining all the relevant information into a single measure may be obtained from the field of fuzzy logic. Klir et al. [58] describe the process of "fuzzy decision making" that applies in situations such as these, and Clark and Yuan [59] have previously used the method to detect the edges of turbulent spots in a transitional flowfield consistent with a turbine blade. Further details regarding decision making with fuzzy sets can be found in Zimmermann [60] and Klir and Yuan [61]. The process employed here is described below along with complete details of the convergence assessment method.

2.3   A Method for Unsteady Convergence Assessment

It is useful to describe the details of the current method with respect to example periodic-unsteady simulations. One machine that is convenient for this purpose is the AFRL High Impact Technologies Research Turbine (HIT RT). An early design iteration of the turbine, denoted here as HPT1, is described in detail by Johnson [62]. The geometry is a single-stage

high-pressure turbine consistent with an engine cycle envisaged for 2017 and beyond. The vane and blade airfoil counts of HPT1 are 22 and 44, respectively. The turbine was analyzed via the 3D time-accurate Reynolds-Averaged Navier Stokes (RANS) solver of Dorney and Davis [63], which is itself a further development of the Rai code [5, 64].

The turbine geometry is shown in Fig. 2.1 as the portion of the wheel (1/22nd) modeled in the simulation, and the operating conditions of the turbine are listed in Table 2.1. Colorization of the non-slip surfaces in the figure is based on instantaneous static pressure. The wheel speed at conditions consistent with a short-duration rig experiment for design-system code validation in the AFRL Turbine Research Facility [65, 66] is 7050 rpm, and with 1/22nd of the annulus modeled the expected periodicity occurs on an interval equal to approximately 0.387 ms. This interval corresponds to one vane-passing per blade or the passage of two blades per vane. At the time-step depicted in Fig. 2.2, the simulation had completed approximately 19 periodic cycles (vane passings), and the time-varying pressure at the location indicated on the blade pressure side for the 2 subsequent cycles is plotted in Fig. 2.2a. While a surface static pressure on the blade pressure side is used in the present example, it is possible to use the method with any flow variable at any location of interest in the domain that is relevant to the design issue at hand.

Table 2.1 Operating conditions for a pair of example turbines.

	Re (1V,exit)	Vane M_{exit}	Blade M_{exit}
HPT1	2.4×10^6	0.82	1.40
HPT2	2.0×10^6	0.75	0.94

All signal-analysis operations required to apply the convergence-assessment method are illustrated in Fig. 2.2a-2.2e. Again, these are the calculation of the time-mean of the flow quantity over each periodic cycle, the Discrete Fourier Transform (DFT), the cross-correlation coefficient (CCF), and the power spectral density (PSD). In keeping with the nomenclature of [56] the time-mean of the static pressure over a single periodic cycle is

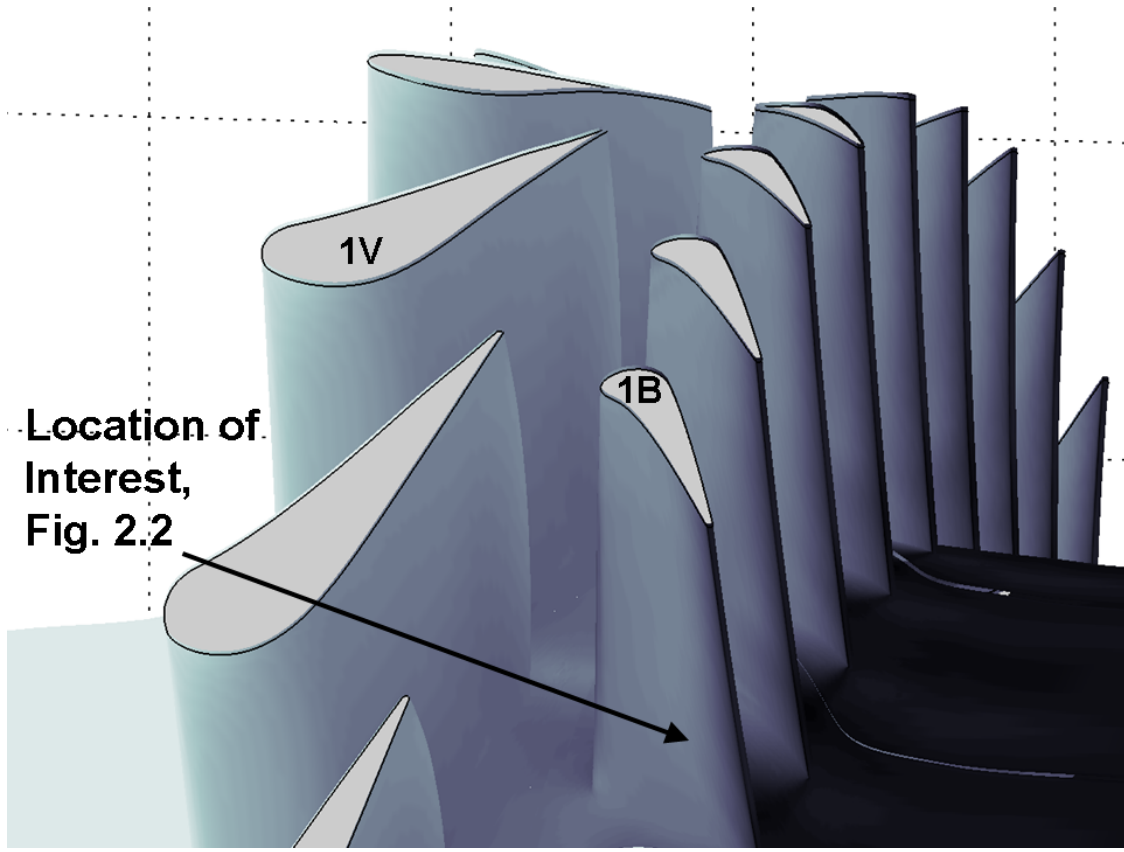$$\bar{p} = \frac{1}{N} \sum_{n=0}^{N-1} p(n+1)$$

$$(2.1)$$

Fig. 2.1   The High Impact Technologies Research Turbine

where N is the number of times steps per period and $p(n+1)$ is the static pressure calculated at an integer multiple, $n+1$, of the time step, Δt. In Fig. 2.2(a) the time-mean levels calculated over each of the two periodic cycles are plotted as well as the raw pressure trace. Complete convergence of the time-averaged signal is achieved when there is no difference in signal mean from one periodic interval to the next.

The Discrete Fourier Transform of the fluctuating pressure, p', evaluated at an integer multiple, k+1, of the signal sampling frequency, $\Delta f = (N \Delta t)^{-1}$ is given by

$$P(k+1) = \sum_{n=0}^{N-1} p'(n+1) e^{-i\frac{2\pi k n}{N}}$$

(2.2)

where Fourier components are defined for values of k between 0 and N-1. Each Fourier component is a phasor, and the time-periodic fluctuation at a given multiple of the sampling frequency can be reconstructed by

$$p(t) = \mathrm{Re}\left\{A e^{i(\omega t + \phi)}\right\} = A\cos(\omega t + \phi)$$

(2.3)

In Equation 2.3, A is the normalized DFT magnitude and Φ is the phase angle, given by
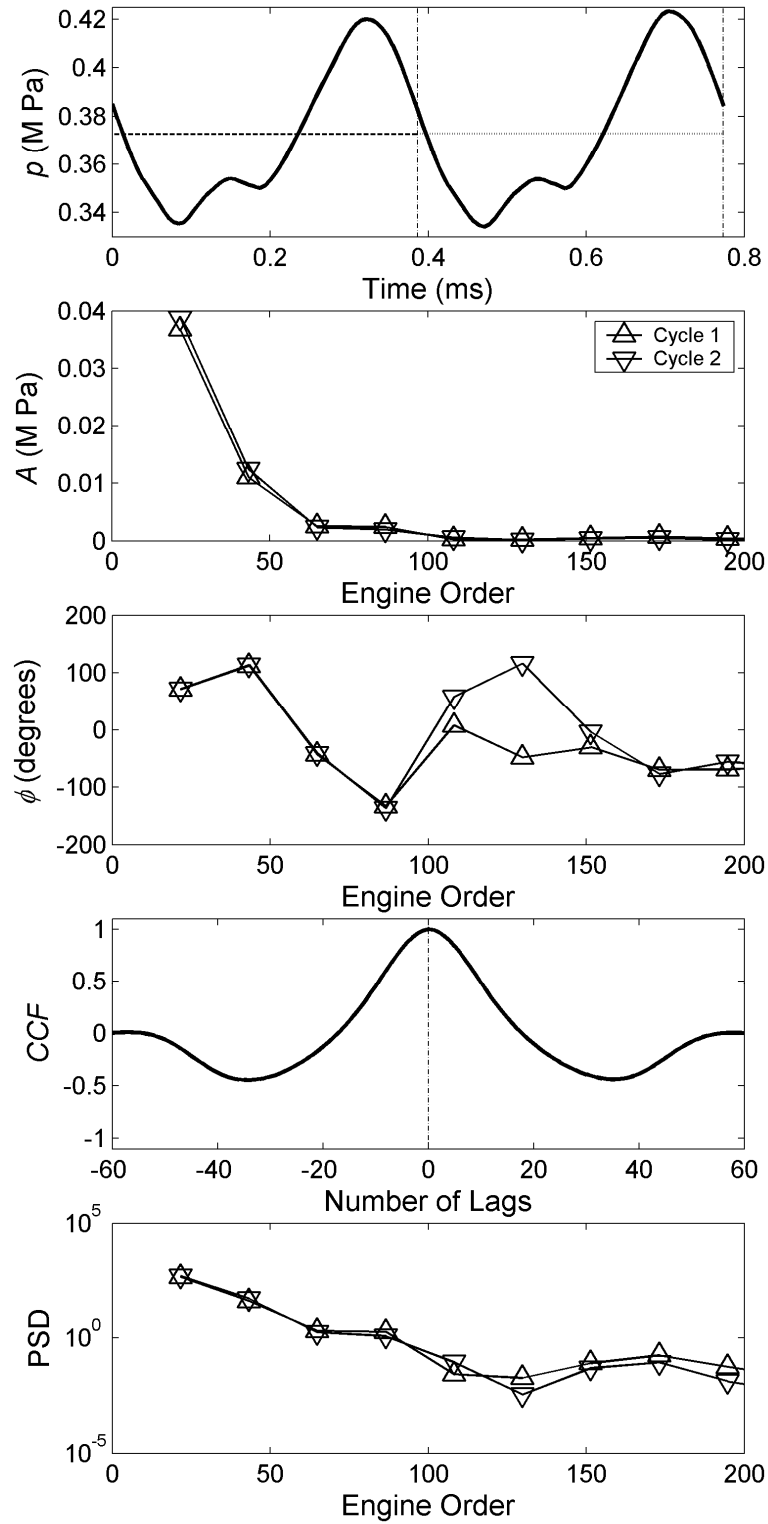
Fig. 2.2   An example of digital signal processing techniques used in the current method for HPT1: (a) time mean; (b) DFT magnitudes; (c) phase angles; (d) cross-correlation coefficients; and (e) power-spectral densities.

$$A = 2\left(\text{Re}^2 + \text{Im}^2\right)^{\frac{1}{2}} / N \quad ; \quad \phi = \tan^{-1}\left(\text{Im}/\text{Re}\right) \tag{2.4}$$

respectively. Also, ω is the circular frequency corresponding to the integer multiple of the sampling frequency, $2\pi\,\Delta f\,(k+1)$. DFT magnitudes and phase angles are plotted in Figs. 2.2(b) and 2.2(c), respectively for each of the periodic intervals plotted in Fig. 2.2(a). Convergence of the simulation at a given frequency is complete when there is neither a change in magnitude nor a difference in phase between the DFT results for two consecutive periodic intervals at frequencies of interest to the designer.

The results of a cross-correlation of the signals from the two periodic cycles of Fig. 2.2(a) are plotted in Fig. 2.2(d). In the time domain the cross-correlation coefficient (*CCF*) is given by

$$CCF(L) = \frac{\dfrac{1}{N}\displaystyle\sum_{n=0}^{N-1} p'\big((n+1) + L\big)\, p'\big((n+1) + N\big)}{\dfrac{1}{N}\left[\displaystyle\sum_{n=0}^{N-1} p'^2\,(n+1)\ \sum_{n=0}^{N-1} p'^2\big((n+1) + N\big)\right]^{\frac{1}{2}}} \tag{2.5}$$

The calculation at a given time lag, L, is accomplished first by multiplying the time-lag-shifted fluctuating pressure over the first interval by the fluctuating pressure signal for the second periodic interval, summing products, and then dividing by the number of samples per period. The result is then normalized by the product of the root-mean-square levels for the two signals. Complete convergence of the unsteady simulation yields a cross-correlation coefficient equal to 1 at zero lag. This implies that the signals from the first and second periodic intervals are exactly alike and that N is the true period of the signals.

The power spectral densities (PSD) of the signals from the two periodic intervals plotted in Fig. 2.2(a) are shown in Fig. 2.2(e). The PSD at a given multiple of the sampling frequency is defined as the product of the Fourier component at that frequency and its complex conjugate divided by the number of samples, N. Convergence of a time-resolved turbomachinery simulation occurs when a large fraction of the overall signal power occurs at frequencies of interest and when that portion of the mean square does not change from one periodic interval to the next.

It is useful to calculate a single parameter that can be used to gauge the level of convergence of the simulation, and multi-valued logic provides a convenient means of accomplishing this objective [58]. One can use the calculated time-mean levels, DFT magnitudes and phase angles, cross-correlation coefficients at zero lag, and fraction of overall signal power at frequencies of interest to define a series of fuzzy sets that express various aspects of the degree of convergence. These fuzzy sets are as follows

$$f_M = 1 - \left| 1 - \frac{\bar{p}_2}{\bar{p}_1} \right| \tag{2.6}$$

$$f_A = 1 - \left| 1 - \frac{A_2}{A_1} \right| \tag{2.7}$$

$$f_\phi = 1 - \left| \frac{\phi_2 - \phi_1}{\pi} \right| \tag{2.8}$$

$$f_S = \left| CCF(0) \right| \tag{2.9}$$

$$f_P = \frac{\sum\limits_{k_{\text{expected}}} PSD(k+1)}{\sum\limits_{k=0}^{N-1} PSD(k+1)} \tag{2.10}$$

where the subscripts 1 and 2 refer to the first and second cycles, respectively. Evaluation of Equations 2.6-2.10 give membership grades in fuzzy sets that describe consistent mean level, amplitude, phase angle, overall signal shape, and fractional signal power, respectively. The amplitude and phase membership grades of Equations 2.7 and 2.8 are calculated for each frequency of interest as defined, for example, by an airfoil Campbell diagram. The numerator in Equation 2.10 is a summation over all frequencies expected to produce significant signal power in the simulation. A level substantially less than 1 implies the presence of either inherent unsteadiness in the simulation or a significant signal level due to some higher harmonic of the expected fundamental frequencies.

The overall convergence level is then itself a fuzzy set defined as the intersection of the others, and this is in turn given by the standard fuzzy intersection [58].

$$f_C = f_M \cap f_A \cap f_\phi \cap f_S \cap f_P = \min(f_M, f_A, f_\phi, f_S, f_P) \tag{2.11}$$

Here we define $f_C \geq 0.95$ for two consecutive cycles to be consistent with convergence of the periodic-unsteady flowfield. To continue this example, Equations 2.6-2.11 were evaluated for the signals plotted in Fig. 2.2, and the results are shown in Table 2.2. For this simulation, significant unsteadiness was expected to occur due to the fundamental vane-passing frequency (22E) as well as two harmonics of that frequency (44E and 66E). Note that more than 99% of the overall signal power is contained in the expected frequencies, so there is not any significant inherent unsteadiness evidenced in the signal. Also note that the signals are 99.9% correlated between the two periodic intervals, so the overall signal shape is very well converged. There is very little phase difference between cycles at the frequencies of interest, and the variation of amplitudes between cycles is greatest for the first harmonic of the fundamental. As a consequence, the overall convergence level of the simulation is 0.886, and this is dictated by the change in amplitude of that engine order (44E) from cycle to cycle.

Table 2.2 Results of the fuzzy-set convergence analysis as applied to the signals in Fig. 2.2.

Fuzzy Set	Membership Grade
f_M	0.999
f_A (22E)	0.947
f_Φ (22E)	0.991
f_A (44E)	0.886
f_Φ (44E)	0.990
f_A (66E)	0.933
f_Φ (66E)	0.988
f_S	0.999
f_P	0.997
f_C	0.886

At this point, it is worth noting that the fuzzy sets f_M and f_S taken together are akin to the sort of information that an "expert user" of unsteady CFD employs to judge the convergence of a simulation. Such an expert would typically plot the time-variation of flowfield quantities for two or more periodic cycles and make a judgment as to how alike the DC and AC components of the signal are from one cycle to the next. In this example, there is very little change in both the time-mean level and the overall signal shape between the cycles plotted in Figure 2.2. An expert user would undoubtedly come to the same conclusion from a visual inspection of the pressure trace plotted in Figure 2.2(a). However, one can see in Table 2.2 that the amplitude of the first harmonic of vane passing is still changing significantly over the two periods plotted in Figure 2.2(a). Since simulations of this type are often performed to assess vibratory stresses during the design cycle of an engine, there is a clear advantage to the application of a more robust method of convergence assessment like that described here. For example, an 11% variation in the amplitude of unsteady forcing could well mean the difference between passing and failing an FAA certification test for resonant stresses.

To complete this example, Figure 2.3 is a plot of the fuzzy convergence level versus the periodic cycle number for 34 periodic intervals (i.e. 34 vane-passing events). The fuzzy sets that dictate the outcome of the overall level are also indicated on the figure. One can see that the convergence behavior of the simulation is in this case controlled by the variations of the magnitude and phase of harmonics of the fundamental from cycle-to-cycle. While this convergence behavior is typical of simulations where simple vane-blade interaction effects dominate the flowfield, the importance of tracking more than the Fourier components as the solution progresses is illustrated below with reference to other turbine geometries.
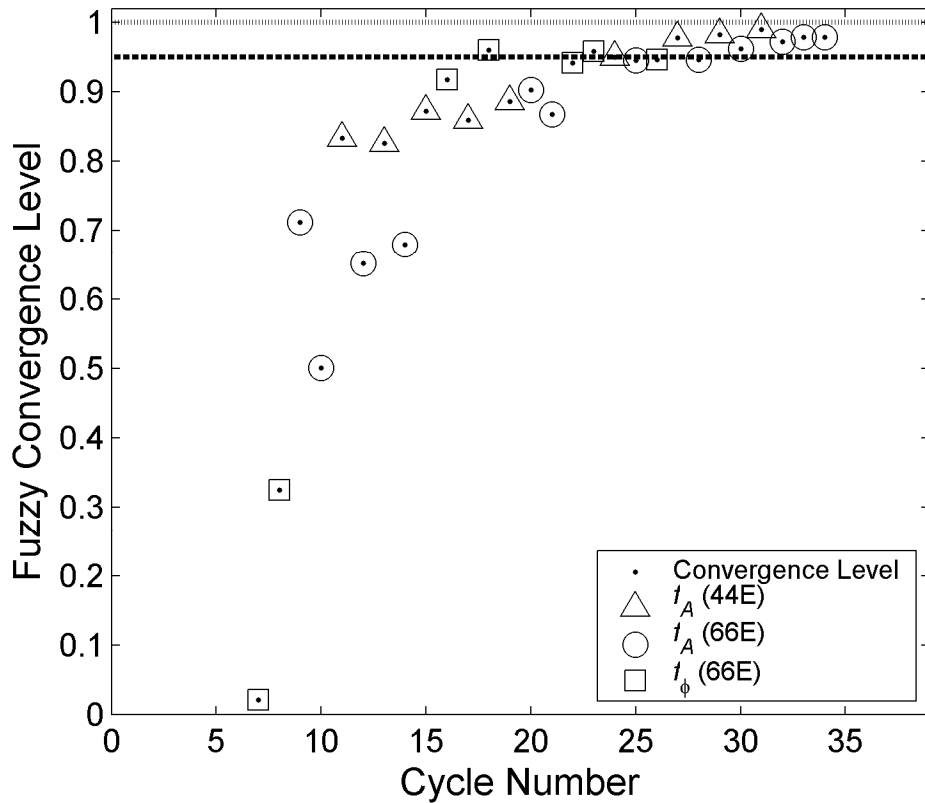
Figure 2.3: Convergence behavior of the flowfield at the location of interest given in Fig. 2.1 for HPT1.

Again, it is important to recognize that the flowfield parameter selected for convergence monitoring is case dependent: the most important quantities are dictated by the reasons for performing the simulation. If the designer is assessing the expected level of resonant stress due to a specific forcing function on the airfoil surface, then the amplitude and phase angle at that frequency must be monitored at a number of locations on the airfoil surface. Alternatively, the amplitude and phase angle of the integrated aerodynamic load on the surface can be monitored. In addition, if the purpose of the analysis is to quantify a change in the time-mean performance resulting from the latest design iteration, then the mass- or mixed-out-averaged efficiency of the stage is the quantity to monitor.

One must also keep in mind that some quantities within the simulation converge well before others: for example, the pressure field typically becomes truly periodic well in advance of the entropy field due to the disparate propagation rates of finite pressure waves and viscous disturbances. So, great flexibility was built into the implementation of the convergence-assessment algorithm described above. The user can monitor a large number of flow quantities at any point in the flowfield. This is very useful when determining overall simulation convergence in post-processing mode. Also, one can estimate the convergence of arbitrary signals generated as the solution progresses (e.g. mass-flow rates, efficiencies, integrated airfoil loadings, etc.), and that can be used to control an unsteady optimization routine. Another example of the application of this algorithm to a periodic-unsteady flowfield predicted in the course of a resonant-stress analysis of a turbine is described below.

2.4   An Example of Atypical Convergence Behavior

Again, a primary reason for executing an unsteady CFD simulation during the turbomachinery design cycle is to predict airfoil resonant stresses. If vibratory stress problems are detected early enough during detailed design, then they can be mitigated, as we shall see later. However, if unacceptable vibratory stresses are discovered after the engine has been put into service, then life-cycle costs can increase significantly. Avoidance of these so called "design escapes" is thus critically dependent upon accurate predictions of unsteady loads on airfoil surfaces.

Predictive tools for vibratory stresses typically rely on accurate Fourier analysis of time-resolved pressure fields [13, 14], and true periodicity is required to avoid errors resulting from spectral leakage [55]. Thus it is necessary for designers to quantify convergence levels prior to determining vibratory stresses, especially when such calculations require the transfer of files between analysis groups (e.g. aerodynamics and structures). Airfoil surface static pressure fluctuations are the root cause of vibratory stresses, and when integrated over the airfoil surface, these static pressures provide the airfoil loading. So, time-resolved traces of the integrated airfoil loading provide a suitable means to monitor convergence in such situations.

For another example of the performance of the present method, consider a stage-and-one-half calculation for a high-pressure turbine (HPT2) having airfoil counts equal to 36, 72, and 48 in the first vane, first blade, and second vane row, respectively. Again, $1/12^{th}$ of the wheel was modeled in the simulation with the purpose of the analysis to assess drivers due to the fundamental vane-passing frequencies only. The solution was run for 6 complete cycles from convergence of the steady-state flowfield, and inspection of Figure 2.4 reveals that convergence was not achieved on that interval in the current example. In fact, a convergence level of less than 0.7 was achieved for the axial force component.

Since the level of convergence achieved by the axial component was lower than that of all the others, it was selected for further investigation. Figure 2.5 is a plot of the normalized axial force signal as well as the membership grades in the fuzzy sets defined in Equations 2.6-2.10 as a function of periodic cycle number. The convergence level is dictated by the lowest membership grade over all the membership functions, namely, the fractional signal power, f_P. A low level of f_P implies that there is significant unsteadiness due to an unexpected frequency. Also note that low levels of the cross-correlation at zero lag, f_S were obtained. This implies a significant change in signal shape from cycle-to-cycle, and this can mean that the primary periodicity occurs in the simulation over some unanticipated time-scale, calling into question the validity of the DFT results used throughout the method. In any case, the results suggest that rigorous interrogation of the unsteady flowfield predicted in the turbine is warranted.
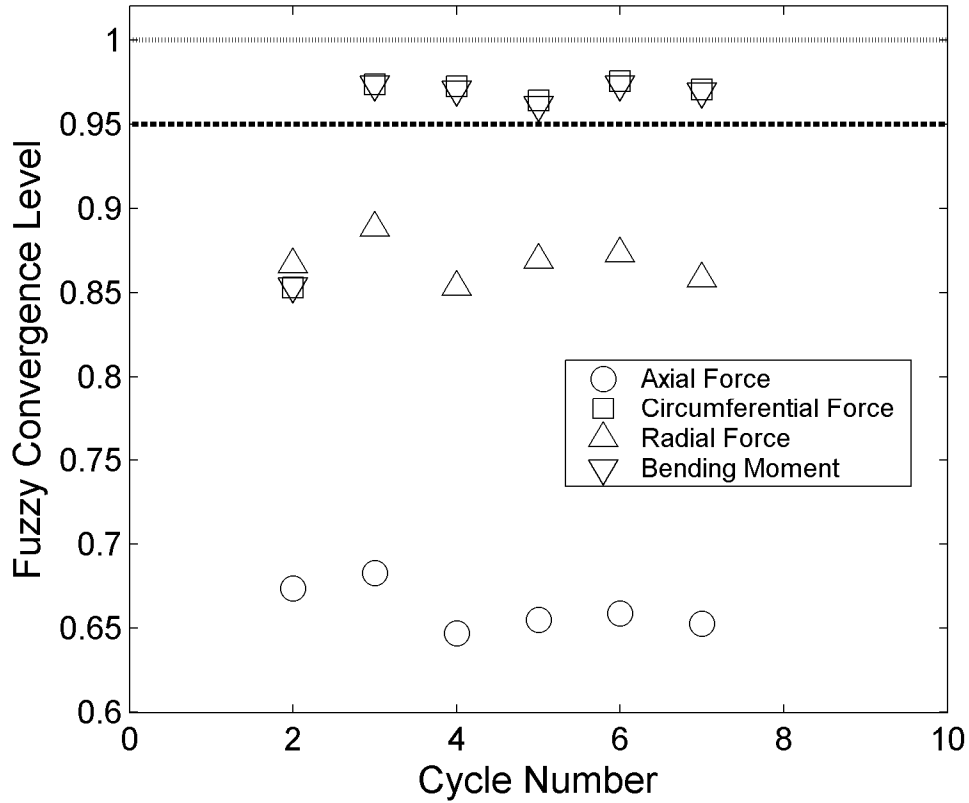
Fig. 2.4 Convergence levels for blade force components as a function of periodic cycle for HPT2

Figure 2.6 is a plot of fractional signal power due to engine orders of excitation up to 300. There is significant unsteadiness in the axial force exerted on the blade due to the first harmonic of the second-vane passing frequency, and this contributes to the low level of f_P. Consideration of the blade Campbell diagram might lead one to conclude that no resonance is to be expected due to that forcing function. However, more problematic is the signal power detected at the engine orders above 150. While 180E is the fourth harmonic of the first-vane passing frequency, the significant peak that occurs at 168E is spurious, and it warrants further investigation.
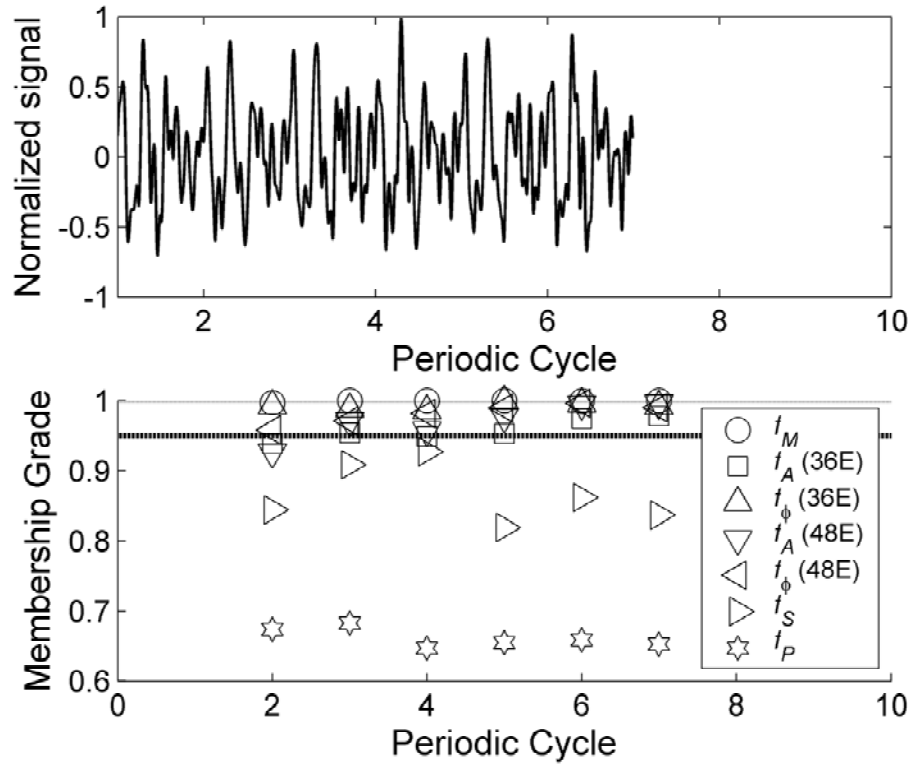
Fig. 2.5   Plots of time-resolved blade axial force and fuzzy-set membership grades as functions of periodic cycle (HPT2).
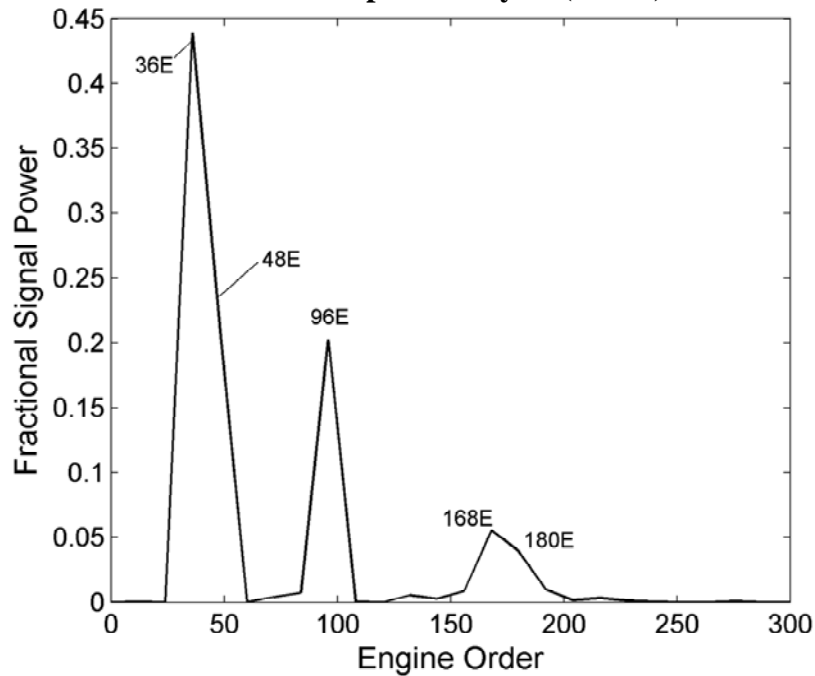

Fig 2.6   The results of a PSD analysis performed on cycle seven of the axial force signal for the blade of HPT2. Power contributions from unexpected frequencies are apparent.

Plots of normalized, time-resolved flow rates entering and exiting the blade row are plotted in Figures 2.7(a) and 2.7(b), respectively, along with fractional signal power as functions of frequency resulting from PSD analysis. One can see the unsteady blockage effect of the upstream vanes very clearly in the inlet flow plots of Figure 2.7. In Figure 2.8, however, there is significant unsteadiness associated with the blockage of the downstream airfoils as well as high-frequency unsteadiness at 168E and 180E. A high-frequency blockage effect is suggestive of inherent unsteadiness (i.e. vortex shedding). Further, the unsteadiness is broad-banded and suggests that the shedding is actually occurring at a frequency between 168E and 180E with an attendant picket-fencing effect on the spectral analysis.
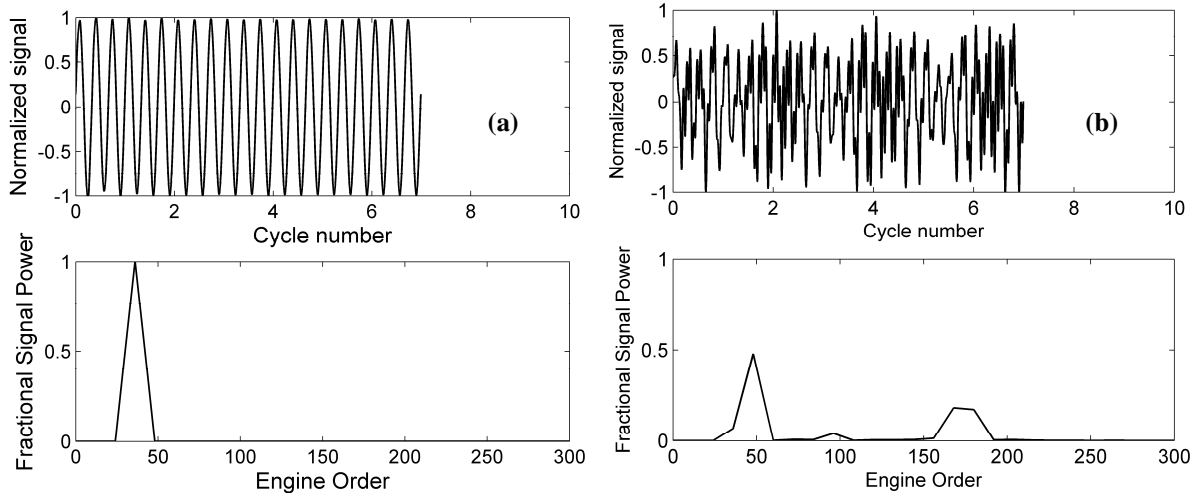

Fig. 2.7   Normalized flow rate (a) into and (b) out of the blade row versus periodic cycle number and the results of a PSD analysis of the signal (HPT2).

One can see additional evidence of vortex shedding in Figures 2.8 and 2.9. Figure 2.8 is a plot of the DFT magnitude calculated from the time-resolved entropy rise through the blade row at 168E ($\approx$ 31 kHz). A midspan plane is shown for a single blade passage, and the highest magnitude of the unsteady entropy rise is found in the vicinity of the blade trailing edge. Again, this is characteristic of vortex shedding. A calculation of the Strouhal number of the oscillations based on trailing-edge diameter and the local velocity in the vicinity of the trailing edge gives a value of $\approx$ 0.16. Figure 2.9 is a plot of the local DFT magnitude of unsteady static pressure at the same midspan plane for the 168E frequency. Very high levels magnitude fluctuations in static pressure occur near the blade throat and downstream of the trailing edge at a location consistent with a reflected cross-passage shock. It is concluded that the unsteady blockage caused by the vortex shedding produces enough of an instantaneous variation in the throat area to cause a shock to form. Consequently exceptionally high levels of unsteady pressure occur on the blade suction side at the vortex-shedding frequency. These unsteady pressure variations would result in severe non-synchronous vibration (a subject often discussed in the literature with respect to compressors [See 67, 68]) in an operating engine.
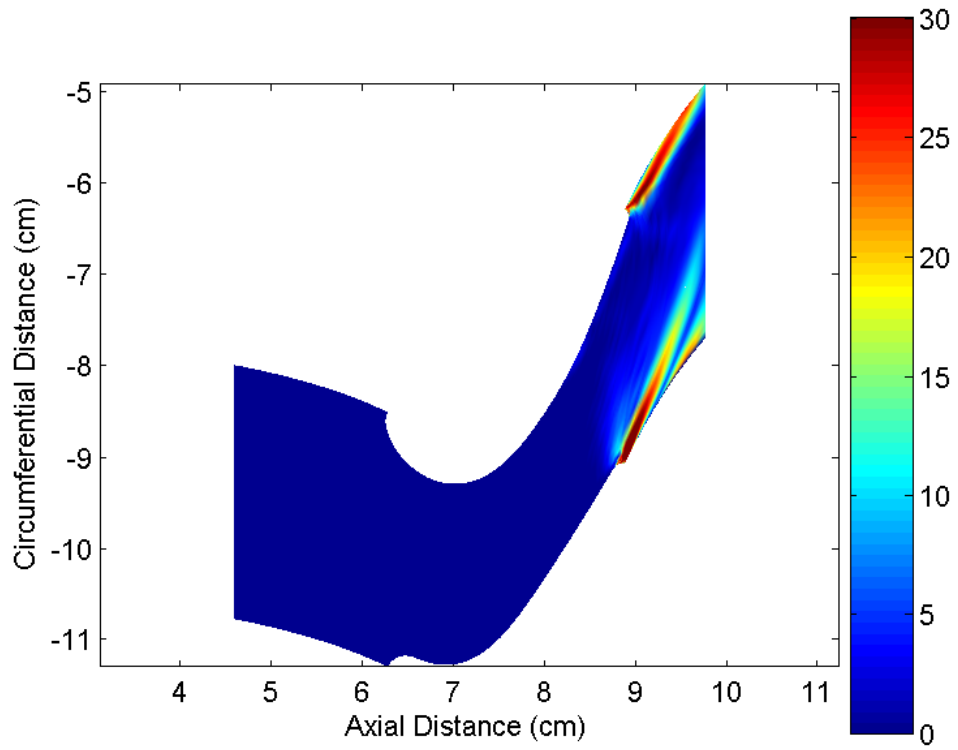
17

Fig. 2.8   Contours of DFT magnitude at 168E calculated from time-resolved entropy rise (J/kg/K) at midspan through the blade passage (HPT2).
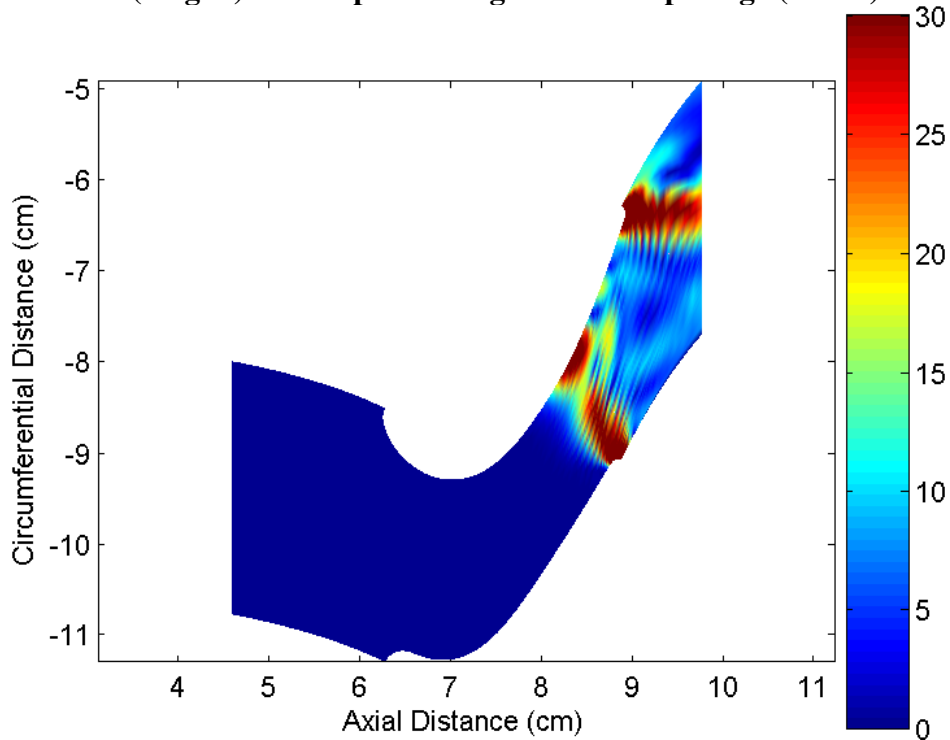

Fig. 2.9   Contours of DFT magnitude at 168E calculated from time-resolved static pressure (kPa) at midspan through the blade passage (HPT2).

18

Note that the simulation described above represents an early iteration in the design cycle for a turbine. In part as a consequence of these results, the design parameters of the turbine changed markedly before the final geometry was obtained. Consequently, no significant high-frequency unsteadiness occurred in the product. So, it is unclear whether or not the phenomenon described here could in fact lead to an airfoil failure. However, Doorly and Oldfield [69] have noted the presence of instantaneous local separation on a turbine blade in conjunction with shock passing, and their Schlieren images were suggestive of the occurrence of the phenomenon described here in the vicinity of the blade trailing edge. In any case, it is clear from this example that application of the present method to assess convergence in predictions of vane-blade interaction provides designers and analysts with significant direction as to the interrogation of the flowfield and the health of the design.

2.4   Conclusions

A quantitative method to assess the level of convergence of a periodic-unsteady simulation was described. The method was based on well known signal-processing techniques, and these were used in conjunction with fuzzy set theory to define a single overall convergence level of the simulation. The development of the method was illustrated with reference to predictions of vane-blade interaction in a pair of transonic high pressure turbines. It was shown that the technique is very useful as an indicator of the overall quality of simulations used to calculate resonant stresses as well as guide to further investigations of the flowfield and characterization of the design. In particular, the method was shown to be useful in detecting inherent unsteadiness in the flowfield of a high-pressure turbine, and therefore judicious application of the technique can be a significant factor in preventing design escapes.

3. Experimental Validation of Predictions for Unsteady Forcing

The importance of validating design-level predictions of time-resolved airfoil loads cannot be over-stated. A demonstrated capability to predict unsteady pressures on airfoils accurately gives the designer confidence in his ability to detect and/or to deter resonant-stress problems in development engines. To have greatest efficacy in reducing life-cycle costs, such code validation is ideally undertaken proactively: verification studies are performed in relevant environments on an ongoing basis whether or not there is a resonant-stress problem in need of solution. This section describes one such study undertaken to assess the effect that airfoil scaling has on predictions of vane-blade interaction in a single-stage HPT. A pair of time-accurate Navier-Stokes analyses was obtained to predict the first-vane/first-blade interaction in a 1+1/2-stage turbine rig for comparison with measurements. In the first computation, airfoil scaling was applied to the turbine blade to achieve periodicity in the circumferential direction while modeling 1/18 of the annulus. In the second, 1/4 of the wheel was modeled without the use of airfoil scaling. For both simulations the predicted unsteady pressures on the blade were compared to measurements from a full-scale turbine rig. The experimentally determined, time-resolved pressures were in best agreement with those predicted with the 1/4-wheel simulation. Thus it was demonstrated that accurate, true predictions of unsteady forcing on the blade due to interaction with the nozzle guide vane were achievable in this flow situation provided that the turbine geometry was modeled rigorously.

3.1   The Turbine Model and Experimental Technique

In this study, the short-duration turbine-test facility at the Gas Turbine Laboratory of the Ohio State University was used to measure the time-averaged and time-resolved surface pressures on airfoils in a full-scale, 1+1/2 stage transonic turbine. The turbine rig (See Fig. 3.1 and Table 3.1) was representative of an early design iteration of the PW6000 engine. The airfoil counts of the model were 36:56:36 in the first vane, first blade, and second vane rows, respectively. The transient facility at OSU, which has been described thoroughly by Dunn et al. [21], was designed to operate as a reflected-shock tunnel, but may also be utilized as a blow-down facility. For this series of experiments, the facility was operated in both modes. However, it was noted that, during the transient test-time, the inlet flow conditions obtained in blow-down mode were steadier than those measured in reflected-shock mode. Since the intent of the experiments was to assess the predictive capabilities of an in-house CFD code at Pratt & Whitney that assumes steady upstream conditions, the time-resolved aerodynamic results presented here were collected when the tunnel was operated in blow-down mode only.
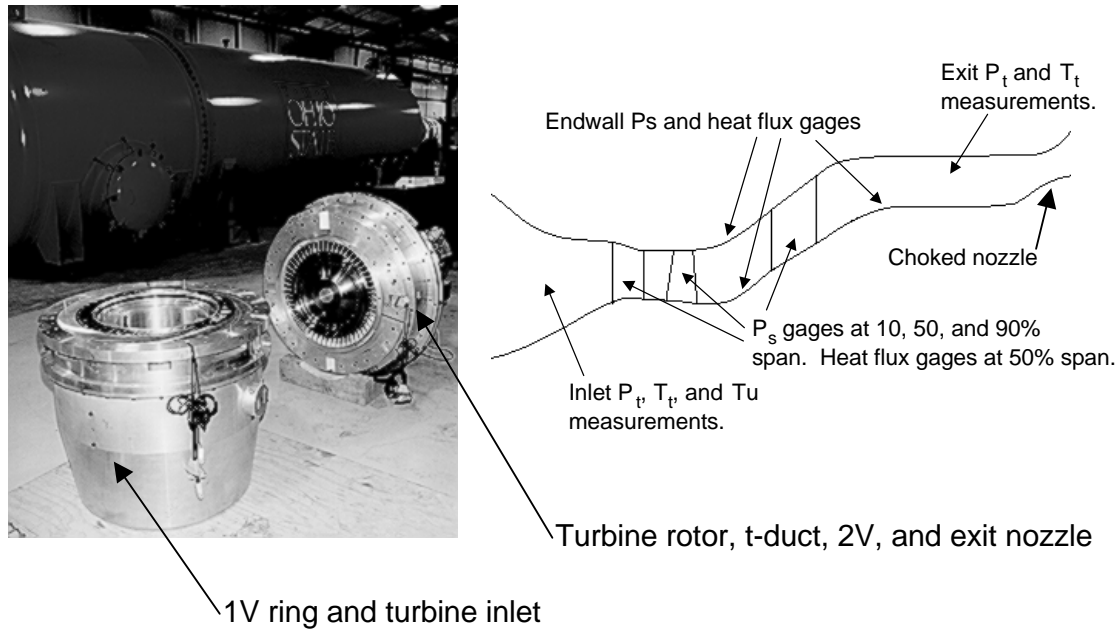
Exit P_t and T_t measurements.

Endwall Ps and heat flux gages

Choked nozzle

P_s gages at 10, 50, and 90% span. Heat flux gages at 50% span.

Inlet P_t, T_t, and Tu measurements.

Turbine rotor, t-duct, 2V, and exit nozzle

1V ring and turbine inlet

Fig. 3.1   The 1+1/2 stage transonic turbine tested at OSU for this study was heavily instrumented on airfoils in each row and along the rig flowpath.

Prior to a tunnel blow-down run, both the driver and driven sections of the shock-tube were filled with air at the same high-pressure (and room temperature) and no diaphragms were used to separate the sections. Therefore, the entire length of the shock tube acted as the driver section of the blow-down runs. Meanwhile, the turbine, which was situated in near-vacuum conditions in the facility dump tank and separated from the driver and driven sections of the tube by a fast-acting valve, was brought to somewhat less than the design speed with an air motor.

Table 3.1 Rig operating conditions, geometric definitions, and details of the time-accurate simulations

Mainflow Conditions :	Design	Measured	
Pt,in / Ps,ex	5.19	5.17	
Speed Parameter (rpm / K 1/2)	421	419	
Inlet Flow Parameter (kg K 1/2) / (Pa s)	7.69x10-4	N/A	
Model Geometry :	1V	1B	2V
Airfoils Per Row	36	56	36
Mean Radius (cm)	29.21	28.98	32.99
Mid-span Axial Chord (cm)	3.07	2.54	5.08
Inlet Mach No. (isentropic)	0.10	0.28	0.48
Exit Mach No. (isentropic)	0.92	1.17	0.71
CFD Models :	1V	1B	2V
Number of Airfoils (1/4 Wheel)	9	14	9
Grid Counts	97x49x57	145x49x57*	161x49x57
Total Number of Grid Points :	>12.3x106		
Number of Airfoils (1/18 Wheel)	2 (36)	3 (54)	9 (36)
Grid Counts	97x49x57	145x49x57*	161x49x57
Total Number of Grid Points :	< 2.7x106		

* Each blade also had a 55x16x16 Tip-Clearance Grid

At the start of a run, the fast-acting valve was opened, and a starting shock was swallowed by the divergent section of a de Laval nozzle until it came to rest as a normal shock just upstream of the turbine-model inlet. The compression-heating associated with the moving shock, total-pressure drop across it, and the increase in wheel speed of the turbine due to work extraction from the flow during the run were all predictable and repeatable. Consequently, the driver pressure, the position of the turbine inlet in the divergent portion of the de Laval nozzle, and the initial wheel speed were all set to achieve the design flow parameter and speed parameter during the run. Additionally, altering the throat area of a choked nozzle downstream of the turbine allowed for the pressure-ratio across the turbine model to be adjusted. During the approximately 100ms run-time of the facility, the upstream area-averaged total pressure and the wheel speed were approximately constant, varying by 8 and 0.6%, respectively over the 40ms interval of data reduced here for a given tunnel run. Both time-resolved static and total pressures were recorded, and instantaneous static-to-total pressure ratios were formed before subsequent data reduction to mitigate the effects of the time-varying upstream total conditions.

As seen in Fig. 3.1, which contains both a photograph of the model and a schematic of its flowpath, the turbine was heavily instrumented both on the airfoils and along the endwalls with flush-mounted Kulite piezo-resistive pressure transducers and thin-film heat flux gages. Total pressures and temperatures were measured on upstream rakes and a downstream

traverse. Also, the leading edge of an upstream circular cylinder was instrumented with heat-flux gages to infer the inlet turbulence-intensity from measurements of the stagnation-point Frossling number (Smith and Kuethe [70]). The turbulence intensity was estimated to be 7±3%, but no inlet turbulence was modeled in the simulations described in the next section.

The main objective of this work was to assess the capability of in-house codes at Pratt & Whitney to predict unsteady forcing functions on blades in transonic turbines. This code validation was of critical importance since designers and analysts need to predict such unsteadiness accurately the first time, every time, if they are to avoid high-cycle fatigue failures during engine development. So, what follows primarily concerns the time-resolved pressure measurements on the first blade of the turbine model at 10, 50, 69, and 90%. For each tunnel run, all unsteady pressures were sampled simultaneously at 100 kHz using a 12-bit data-acquisition system. Each transducer had an active sensing area of 0.64mm by 0.64mm, and all sensors were calibrated throughout the entire data system at regular intervals during the test program. Further details of the calibration technique and typical results were reported by Dunn and Haldeman [4].

3.2 Computational Methods

The time-mean and time-resolved unsteady pressure fields in the 1+1/2 stage transonic turbine were predicted using the 3-D, multi-stage Reynolds-Averaged Navier-Stokes code described collectively by Ni [33], Ni and Bogoian [34], and Davis et al. [35]. The code employs implicit dual time-stepping to solve for the periodic-unsteady flowfield on an H-grid, and numerical closure is obtained via the Baldwin-Lomax [71] turbulence model. The code is accurate to second-order in both space and time. The flow solver employs a finite-volume, cell-vertex Lax-Wendroff [72] method, and both local time-stepping and multi-grid techniques are used to obtain rapid convergence. For time-accurate calculations of rotor/stator-interaction with the Ni code, the flowfield is solved on a portion of the annulus over which spatial periodicity occurs.

For the model turbine of this study, with airfoil counts of 36:56:36, circumferential periodicity occurred on 1/4 of the wheel, so a time-accurate solution of the 3-D flowfield required a model having airfoil counts of 9:14:9, as seen in Table 3.1. The grid counts used for each airfoil passage are also listed in the table, and these are consistent with grids used during the design process at P&W. The P&W design viscous-grid provides values of y^+ less than 5 over all airfoil surfaces as recommended by Dunham and Meauze [73] for use with mixing-length turbulence models. Also, the grid gives approximately 10 grid points in the boundary layer on each airfoil surface and 20 grid points in the wakes near the airfoil trailing edges.

Note that the total number of grid points needed for the 1/4-wheel model was in excess of 12.3 million. However, if a modicum of blade scaling was used (See Fig. 3.2 and Table 3.1), and the airfoil counts were changed to 36:54:36, a 2:3:2 model could be employed over 1/18 of the annulus. For the same grid density, less than 2.7 million grid points were required. This was a considerable reduction in computational resources, and such scaling was utilized during the design phase of the rig and to decide the placement of sensors on the turbine surfaces.
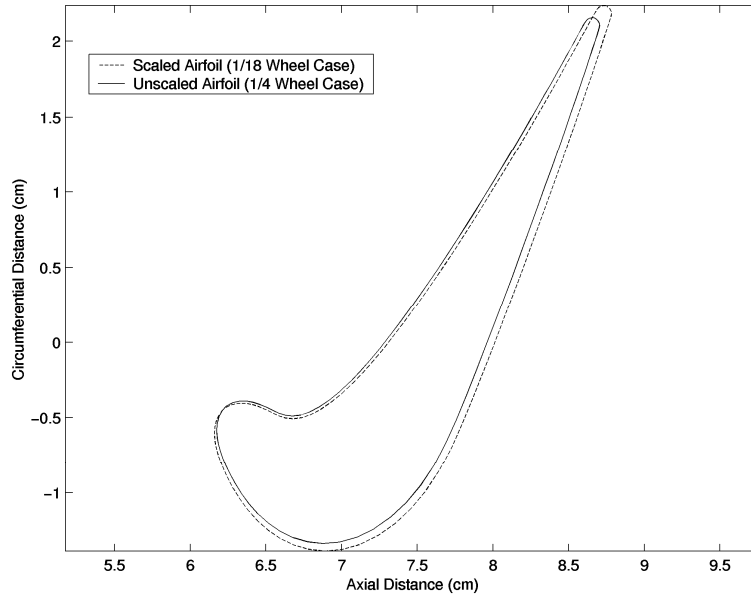
Fig. 3.2   Mid-span blade geometries for the 1/4-wheel and 1/18-wheel simulations.

Since the turbine rig described above was modeled both with and without the use of blade scaling, this combined experimental/computational study provides a unique database with which to examine the effect of scaling on predicted unsteady pressures in the transonic turbine. As a result of this exercise, one may conclude whether or not accurate assessments of unsteady forcing on an airfoil are possible during the design cycle if simplified airfoil-counts are modeled. To bring each simulation to convergence, the global time-step was set such that the Nyquist frequency was approximately 500kHz, and the solutions were post-processed in a way that mimicked the experiment. That is, the CFD solution was "sampled" at a data rate of approximately 100kHz (i.e. 50kHz Nyquist frequency [55]). For the unscaled blade, the time-history of 1/4-revolution was recorded, and this was compared to 4 global cycles of the 1/18-wheel case. In this way, the time-resolved pressures from each case had comparable spectral resolutions, and both spectral-leakage and picket-fencing effects were avoided in the frequency domain.

3.3   Time-Mean Blade Loadings

Prior to the experimental program, predictions of the unsteady flowfield in the rig were made at design conditions. That is, the simulation results to follow represent true pre-test predictions. The geometry of each of the 36 vanes in the nozzle guide-vane row was measured, and then the average airfoil was modeled for each vane in the prediction. Similarly, each blade was assumed to have the mean shape of four measured airfoils, and the design-intent flowpath and second vanes were simulated. Both the 1/4-wheel and 1/18-wheel simulations were executed prior to the test program. For the 1/18-wheel simulation, the scaled airfoil was shifted axially to hold the 1V-1B midspan axial gap, and the 1V inlet flow parameter (and hence inlet Reynolds number) was also kept constant. Figures 3.3(a)-3.3(c) are plots of predicted unsteady envelopes for 10, 50, and 90% span on the 1B, respectively, for both the scaled- and true-count analyses. The 1/4-wheel and 1/18-wheel predictions are in very good agreement. This gives some credence to the idea that minimal airfoil scaling such as that used in the 1/18-wheel simulation yields adequate predicted levels of unsteadiness.

24

The predictions in Fig. 3.3 are also compared with the peak-to-peak variations and time means of ensemble-averaged experimental pressures. In general, the unsteady envelopes compare well with the predicted peak-to-peak levels. This means that the unsteady interaction with the average vane is well predicted. However, the time-mean blade loading measured in the experiment is not in as good agreement with the prediction for the average blade. Again, only 4 blades out of 56 were used to define the CFD model. Also, there is some apparent unloading of the blade at 90% span. Upon further examination of the sensor logs for the experimental program, it was found that calibration difficulties were experienced for the Kulite at 30% axial chord on the blade suction side. Consequently, systematic errors are suspected for that sensor, and the data is only plotted for completeness. This leaves just the data from the sensor at 10% axial chord, which is not enough upon which to make a judgment regarding the efficacy of the tip-clearance modeling in the code, for example. Also, the overall the loadings on all airfoils responded as predicted for changes in incidence and pressure ratio. Moreover, the goal of the study is to assess the predictive capabilities of the Ni code for unsteady forcing functions, and so, further discussion and analysis is restricted to time-resolved pressures.
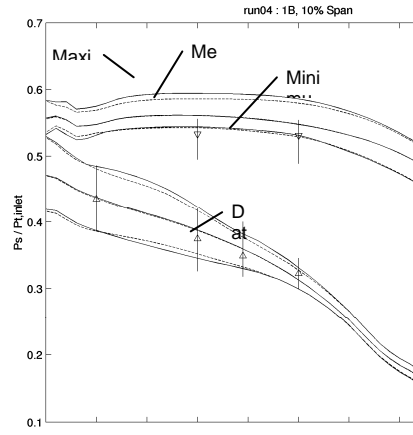
(a)
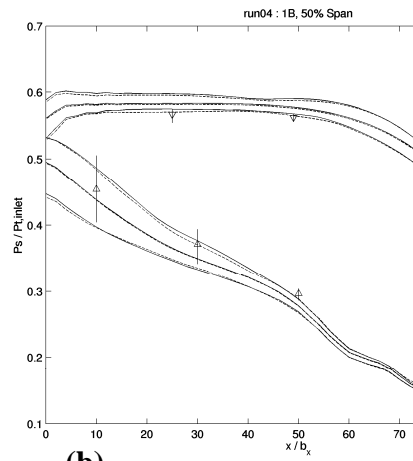
(b)
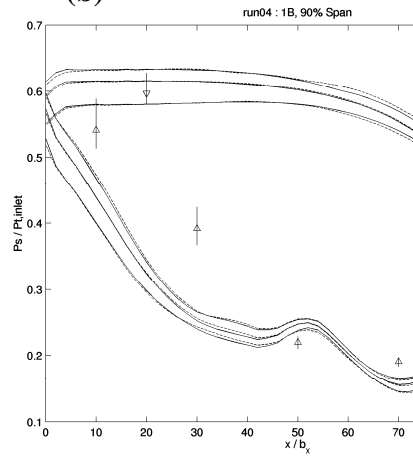
(c)

Fig. 3.3   Unsteady envelopes for the 1/4-wheel (solid lines) and 1/18-wheel simulations (broken lines) at (a) 10, (b) 50, and (c) 90% span on the 1B.

3.4   Time-Resolved Surface Pressures

As noted above, all airfoils are identical in the simulations. However, passage-to-passage variations exist in the experiment, and these necessarily result in discrepancies between the predicted and measured time-resolved pressures. As an example, the unsteadiness on the blade upstream of the cross-passage shock is primarily a consequence of the blade passing though the circumferential distortion in static pressure associated with each upstream airfoil. Each airfoil around the first vane row was found to have a throat area that was normally distributed about the mean value, so the circumferential variation in static pressure downstream of each vane also varied. Consequently, the time-resolved pressure measured at a fixed location on the blade as it makes one revolution behind the vane row should be different from that predicted in two obvious ways. First, the peak-to-peak level of unsteadiness should be greater than that associated with a vane ring composed of identical airfoils. Second, random unsteadiness should be discernible in the measured traces, but not in the predicted ones.

Figure 3.4 is a set of 4 normalized pressure traces associated with the Kulite sensor at 77% axial chord on the 1B pressure side at 10% span. In Fig. 3.4(a), the measured time-resolved pressure is plotted for one quarter of the revolution of the rotor, while in Fig. 3.4(b) the trace predicted by the 1/4-wheel simulation is shown along with a pair of post-processed experimental traces. Note that the peak-to-peak variation in pressure is greater in the raw experimental data than for the prediction, and the unsteadiness is composed of a broader band of frequencies. It is useful, however, to compare the prediction to a measurement of the unsteadiness due to the average vane.

It is possible to reconstitute the periodic-unsteady portion of the signal from the raw trace of Fig. 3.4(a) in one of two ways. Either an ensemble average of the unsteadiness due to each of the 36 vanes is calculated over an integer number of rotor revolutions, or the 36E Fourier components of the measured signal and its harmonics are translated back to the time domain and summed. The results of both of these procedures are plotted in Fig. 3.4(b), and the traces compare very well with the pressure trace predicted for the average vane in terms of both frequency content and peak-to-peak magnitude. Note that there are small differences in phase between the predicted signal and both the ensemble-averaged and reconstructed experimental traces. This is a consequence of discrepancies between the location of the turbine wheel in the experiment and the prediction. Both the experiment and the prediction were sampled at the same data rate (100 kHz). However, the rotors in the simulation and the experiment can only be aligned circumferentially to within +/- 6 x (N Δt) degrees, and this leads to the small difference in phase.

For the signal reconstructed from Fourier components in Fig. 3.4, only the fundamental and first harmonic of the vane-passing frequency were used. Visually, this simplification appears to be adequate, but it is possible to show rigorously that that the 36E and 72E components are the most relevant using signal processing techniques. The theorem of Parseval states that the integral of the power-spectral density of a signal over a range of frequencies yields the contribution of those frequencies to the signal mean-square [55]. Consider Fig. 3.5(a) and 3.5(b), which are contour plots of the percentage of the signal variance obtained by integrating the power-spectral densities of time-resolved pressures at all grid points on the blade pressure and suction sides, respectively over the frequency range 34E-74E (1/4-wheel model). Also plotted on the figures are the locations of the Kulite static-pressure sensors.

27

Note that the vane-passing and twice vane-passing frequencies account for over 90% of the predicted mean-square unsteadiness in static pressure over the entire blade surface. So, using the 36E and 72E frequencies only to reconstruct the experimental trace in Fig. 4(b) is adequate, and it is possible to restrict further comparisons of the 1/4-wheel and 1/18-wheel predictions to those frequencies.
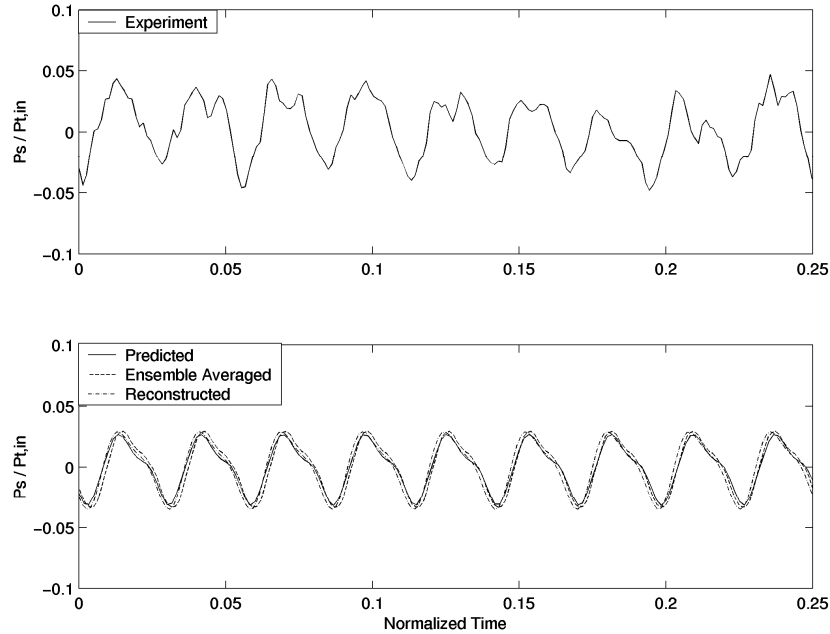

Fig. 3.4   Time-resolved static pressure traces (normalized by upstream total pressure) for a sensor at 10% span and 77% chord on the 1B pressure side. Time is normalized by the period of revolution of the rotor. (a) raw signal, (b) predicted, ensemble-averaged, and reconstructed signals.

In Fig. 3.6, measured and predicted DFT magnitudes on the pressure side of the blade are compared. The contour plots for the blade surfaces are percent difference values between the 1/4-wheel and 1/18-wheel simulations relative to the maximum magnitude of the predicted unsteadiness in the 1/4-wheel case at 36E and 72E. There are significant discrepancies in the DFT magnitudes between the two simulations at both frequencies. At 36E, the differences are most pronounced at the tip, with the 1/4-wheel simulation predicting greater unsteadiness forward of mid-chord and lesser aft than the 1/18-wheel prediction. However, the disparity between the two simulations is more apparent at 72E with the greater unsteadiness predicted near the root for the 1/4-wheel case and less near the tip than that of the 1/18-wheel prediction. The variations of DFT magnitude with engine order are plotted over a range including the fundamental vane-passing frequency and four harmonics for several sensor locations where the largest discrepancies between predictions are found. At 36E, the 1/4-wheel simulation better predicts the distributions of DFT magnitude over the pressure surface measured in the experiment both qualitatively and quantitatively. Also, the 1/4-wheel simulation is conservative with respect to the magnitude of fluctuations at 72E, whereas the 1/18-wheel prediction is anti-conservative. Overall, the 1/4-wheel simulation better represents the physics of the vane-blade interaction in the rig than the calculation in which airfoil scaling was used.
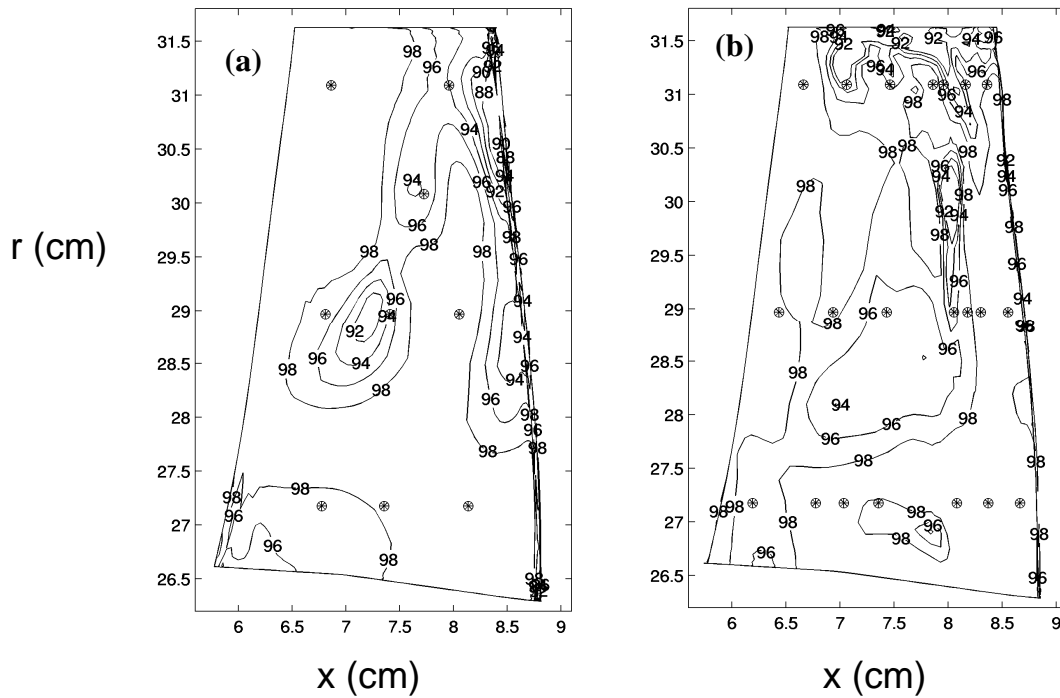
Figure 3.5 Over 90% of the predicted mean-square unsteadiness is contained in the frequency range from 34E-74E on both the (a) pressure and (b) suction sides.

Figure 3.7 is organized similarly to Fig. 3.6. At the 36E frequency the absolute value of the percent difference in predicted magnitude was less than 4% over the entire surface of the blade where sensors were located. The 72E unsteadiness-levels are significantly greater near the root in the 1/4-wheel prediction forward of mid-chord. The distributions of DFT magnitude with engine order are plotted for several sensor locations where the largest discrepancies between the predictions are found. Again, the 1/4-wheel simulation is conservative with respect to the magnitude of fluctuations at 72E, whereas the 1/18-wheel prediction is anti-conservative.
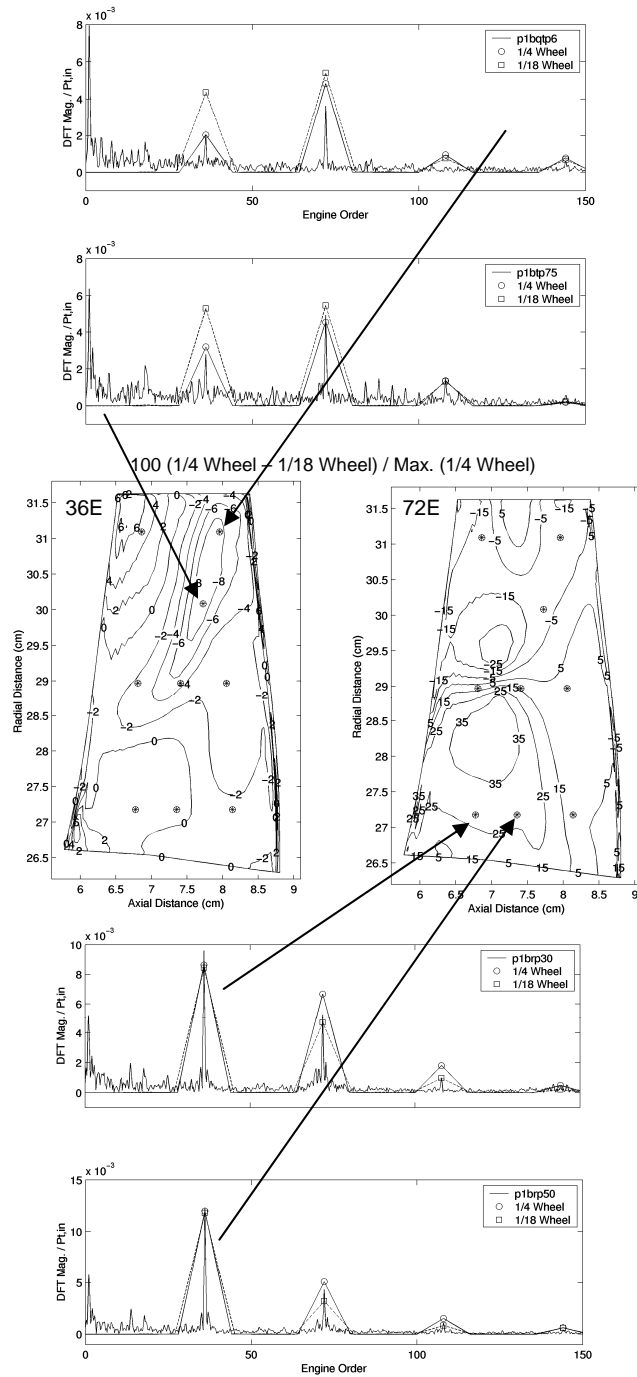
Fig. 3.6   A comparison of measured and predicted DFT magnitudes for the 1B pressure side.
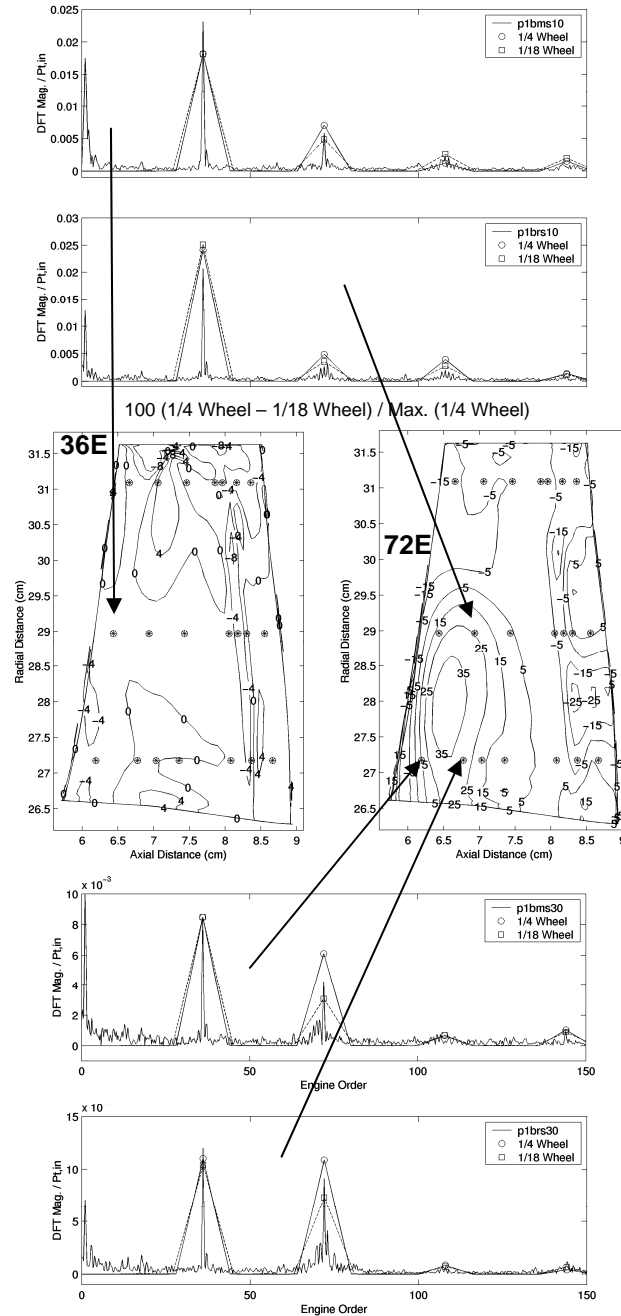
Fig. 3.7   A comparison of measured and predicted DFT magnitudes for the 1B suction side.

The discrepancies in time-resolved blade loadings between the pre-test predictions mean that simulations involving airfoil scaling may result in under- or over-prediction of resonant stresses on excited blades, depending on the vibratory mode of interest. Worse still, when such an analysis is performed during the design process, design changes to alleviate a high level of predicted vibratory stress could possibly have the opposite of the intended effect if the sources of excitation are not well understood. Also, it should be noted that the phase

relationships among unsteady pressures on the turbine blade in the 1/18-wheel simulation are by definition incorrect. So, although one might argue that the differences in DFT magnitudes between the 1/4- and 1/18-wheel simulations are within the expected uncertainty bounds of a typical resonant-stress analysis, it is inadvisable to use the results of a prediction made with scaled airfoils for such a purpose. Unfortunately, given the computational resources often required to perform an unsteady analysis of a turbine with arbitrary counts, designers many times must rely on the results of scaled analyses. That is, a designer typically hopes that the results of scaled analyses are at least trend-wise accurate when judging the relative merits of one design iteration versus another. Again, given the results presented here, that is certainly a dubious practice. A better method for analyzing a turbomachine with arbitrary counts at modest computational cost would involve the use phase-lagged boundary conditions as described, for example, by Chen and Briley [74]. Again, extensive validation is required to use such a tool with confidence in design to mitigate unsteady forcing.

To visualize the mechanisms responsible here for the unsteadiness at each frequency, contour plots of the instantaneous pressure field in the blade passage are given in Fig. 3.8 for a number of time-steps from the 1/18-wheel prediction. Two sets of contour plots are shown, and these correspond to snapshots of the pressure field in the frame of reference of the moving blades. The fluctuating pressures plotted in the contour plots on the left and right have been notch filtered at 36E and 72E, respectively. Application of the narrow-band-pass filters allows visualization of the vane-blade interaction at each of the frequencies of interest in isolation.

Before filtering, the time-resolved pressures in the upstream vane-row were interpolated onto a grid that was fixed in the frame of reference of the blade row. This interpolation was applied only to the data plotted in Fig. 3.8, which was used only to visualize the 36E and 72E vane/blade interaction effects. As a consequence of the interpolation, it was possible to calculate the time-mean static pressure throughout the entire flow-field in the blade frame of reference and to subtract it from the instantaneous pressure. Thus the propagation of pressure waves across the interface was preserved. With the DC level removed, a digital finite-impulse response (FIR) filter that had an exactly linear phase-response in the pass-band was used to accentuate the fluctuations at the frequency of interest [56].
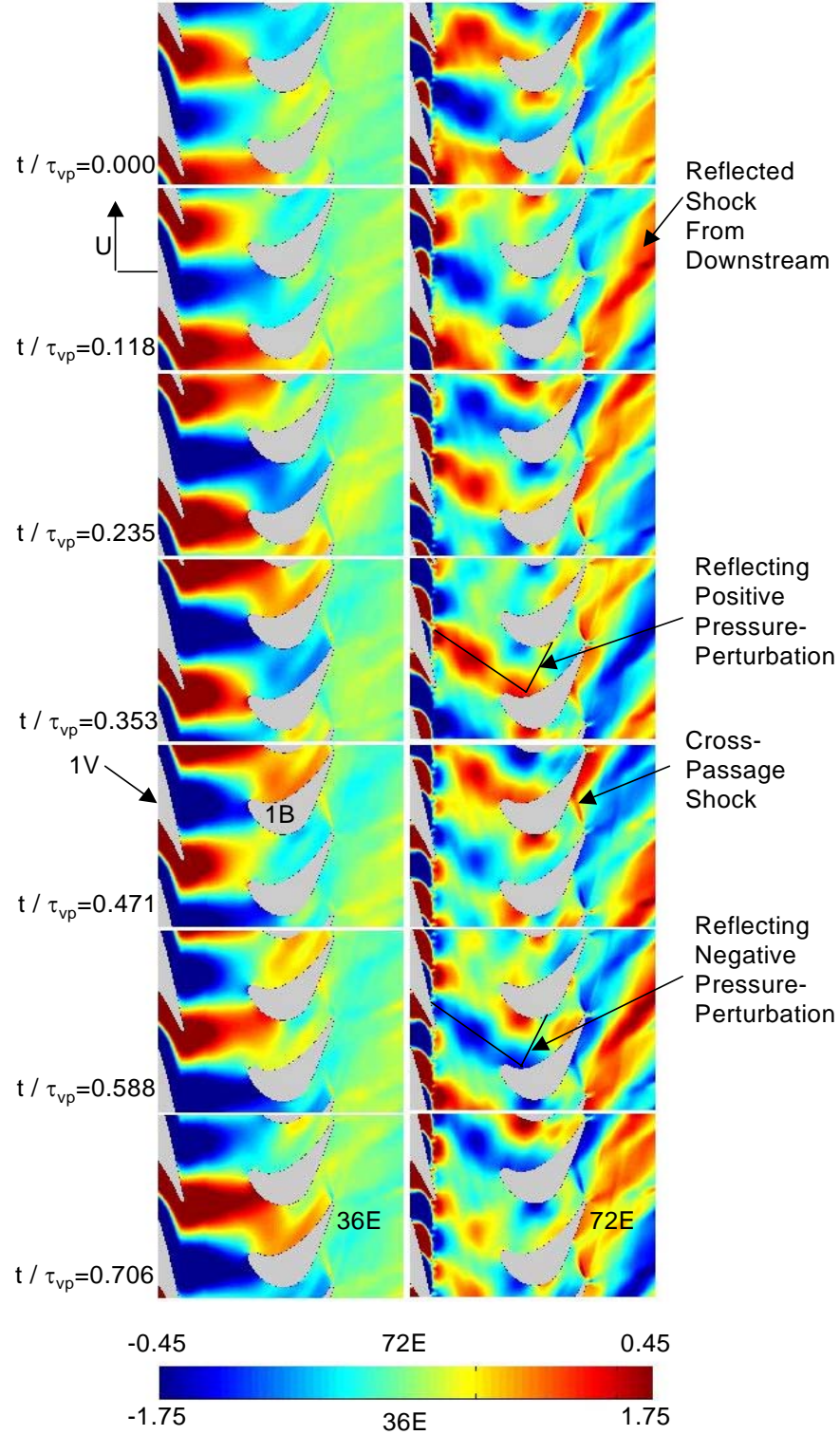
Fig. 3.8 **Instantaneous static-pressure contours in the blade frame of reference. The time-resolved pressures have been notch-filtered at 36E (left column) and 72E (right column) to visualize the unsteadiness due to those frequencies only.**

At each time-step depicted in Fig. 3.8, and for each of the contour plots at a given interval, the cross-passage shock wave is discernible to some degree in the blade passage. Note that no unsteady pressure fluctuations that propagate from the interaction with the upstream vane row penetrate that shock and continue downstream. Also note that there is some unsteadiness at both 36E and 72E which is propagating upstream to the trailing-edge region of the blade suction side. These pressure waves are generated by the reflection of the blade trailing-edge shock from the downstream vane row and transition duct. These waves do not propagate upstream of the cross-passage shock. Thus it may be concluded that the largest discrepancies between the simulations, which occur upstream of the cross-passage shock, must result from differences in the first-vane/blade interaction.

As the circumferential distortion in static pressure associated with the exit of each first-vane passage passes upstream of the rotor, the blades are subjected to alternating positive and negative pressure perturbations. These perturbations are either two or four in number depending upon whether 36E or 72E notch-filtered fluctuations are considered. These sets of perturbations are consequences of the waveform the circumferential distortion in static pressure takes at a given radius. The perturbations give rise to potential interactions that propagate and reflect through the blade row, creating complex interference patterns with each other and in turn interacting with wake events that are convecting with the local freestream. Such interference patterns are heavily dependent on the geometry of the blade passage. This is the reason that the 1/4-wheel and 1/18-wheel predictions, which represent small changes in the blade geometry from case to case, yield different levels of unsteadiness on the blade surfaces, particularly at the 72E frequency where the interference pattern is more complex.

In this turbine, the first-vane/blade interaction is greater in an absolute sense than that of the blade/transition-duct/second vane as far as the blade is concerned. So, the strongest drivers associated with blade high-cycle fatigue for this machine are related to interactions with the upstream airfoil. However, this situation is not universally applicable, and it depends strongly on the reaction of the machine in question as well as other factors such as vane/blade axial gaps, for example. If the design reaction were larger, then the vane- and blade-exit Mach numbers would decrease and increase, respectively. Thus, the interaction of the blade with the second vane might dominate high-cycle fatigue concerns. Such an interaction is interesting and complex for single-stage turbines that have downstream vanes consistent with contra-rotating low-pressure turbines, as is the case here. So, a companion paper that addresses the complex moving-shock-interactions occurring in the transition duct and second vane as a consequence of the passage of the blade is available (See Davis et al. [75]). The accurate prediction of such interactions is also part of an ongoing research effort at the Air Force Research Laboratory.

3.5 Conclusions

The effect of airfoil scaling on predictions of the time-resolved static pressure on the blade surface in a 1+1/2 stage transonic turbine was assessed. Significant differences in the predicted first vane/first blade potential interaction were found, and these were manifested as discrepancies in amplitudes of unsteadiness on both the pressure and suction surfaces of the airfoil, particularly at twice vane-passing frequency. When no airfoil scaling was used and the true airfoil counts were modeled, the predicted levels of unsteadiness on the blade were in very good agreement with measurements in a short-duration turbine rig. Consequently, the predictive method described can be used with confidence both to predict forcing functions for

resonant stress calculations and to discern the mechanics of such interactions provided the geometry of interest is modeled accurately. The results presented here are also pertinent to the design of transonic turbines since time-resolved airfoil loadings are often predicted using CFD models employing scaled airfoils. As a result of this study, it is recommended that analysts not use the results of scaled-airfoil predictions as a basis for design decisions in any attempt to reduce high levels of unsteadiness, particularly at multiples of the relevant passing frequency.

4. Resonant Stress Reduction in Demonstrator Engines

In the previous section, the short-duration turbine-test facility at the Gas Turbine Laboratory of the Ohio State University was used in blow-down mode to measure the time-averaged and time-resolved surface pressures on airfoils in a 1+1/2 stage, full-scale transonic turbine. The main objective of the study was to assess the capability of the design system at Pratt & Whitney to predict unsteady forcing functions on blades in transonic turbines. Consequently, experimental measurements of the magnitude and phase of pressure fluctuations due to the 1V-1B interaction were compared to true pre-test predictions. It was found that both the magnitude and phase of the unsteady forcing function were very well predicted provided that actual airfoil counts were used in the computational model. That is, it was necessary to avoid airfoil scaling if accurate unsteady pressure predictions (and hence unsteady forcing and resonant stress levels) were of paramount importance.

Additional results from the code-validation study are provided in Fig. 4.1 for the 1B pressure side. In the last section it was concluded that in this situation, all unsteadiness on the blade pressure side was a consequence of the interaction of the blade with the upstream vane row. The pattern of unsteadiness plotted in Fig. 4.1 is consistent with what one might expect to be a significant driver of blade vibration in the first-torsion mode. In this section, the results and lessons learned during that investigation are utilized to predict and ultimately to control the first-torsion-mode resonant stress on a single-stage high-turbine blade. The merit of the resulting design changes is confirmed through development-engine tests.
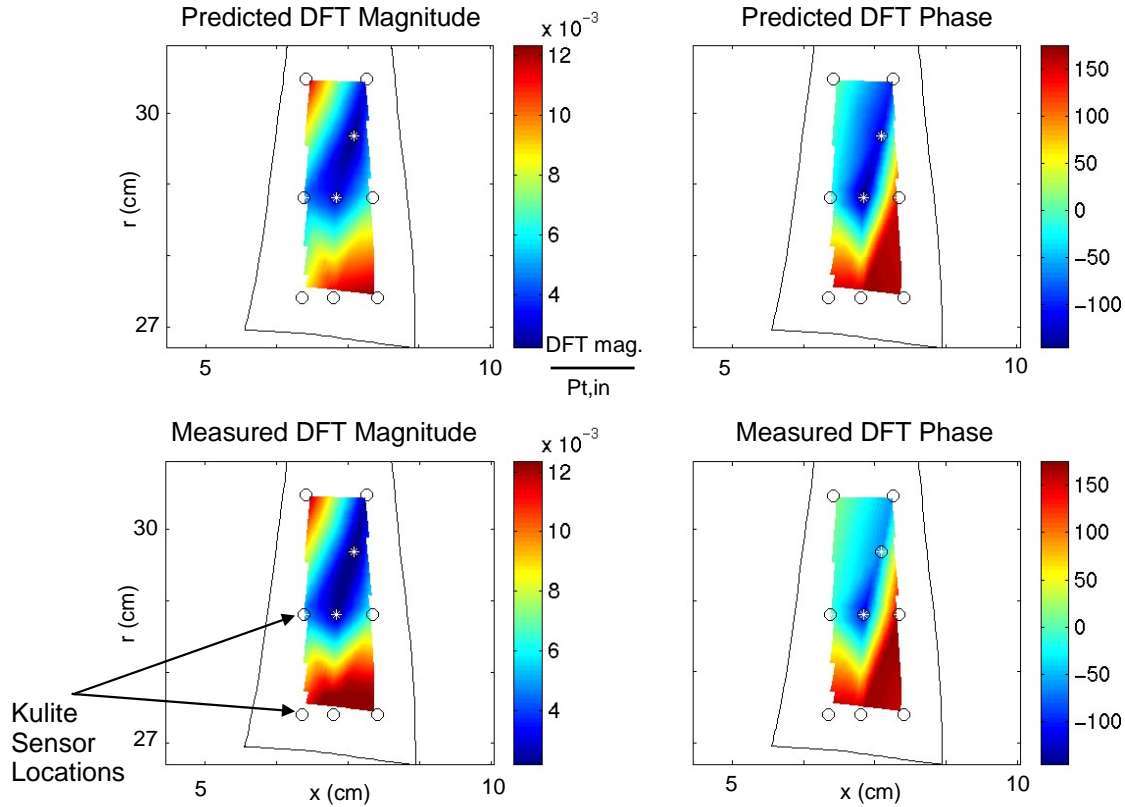
Fig. 4.1   Measured levels of unsteadiness on the 1B pressure side in the 1+1/2 stage transonic turbine rig compared very well with predictions of DFT magnitude and phase.

Subsequent to the experimental and computational study reported in the previous section, a development-engine test resulted in an unacceptable level of measured resonant stress for the third mode (first torsion) of an HPT blade. Since single stage HPT pressure fields are largely scalable across a wide operating range [76, 77], it was possible to apply the lessons learned in the validation study directly and immediately to reduce the level of the resonant stress due to that vibratory mode. Resonant stresses may be reduced either by increasing levels of damping (aerodynamic and/or mechanical) or by decreasing levels of unsteady pressures. Aerodynamically, an attractive option is to reduce the levels of unsteady forcing at the relevant frequency if possible. In this case, the driver for the vibration was the interaction of the nozzle guide vane and the 1B at the fundamental vane-passing frequency. Since it was now known that both magnitude and phase of unsteady forcing could be well predicted with careful analysis under similar conditions, a design effort to reduce the levels of resonant stress on the blade was initiated.   Two methods were chosen to decrease the level of forcing, and each required some redesign of the first vane row. These methods were the use of asymmetric vane spacing and the redesign of the vane suction side using optimization techniques.

Both solution methods hinged on lessons learned during the pretest analysis-phase of the code-validation study. Narrow band-pass filters were used in conjunction with animation techniques to determine that potential-field effects were the dominant source of unsteady pressures resulting from vane-blade interaction in that situation.   Note that the phase-angle results for the first vane passing-frequency (1VPF) that are plotted in Fig. 4.1 are also in keeping with that assessment. Consider the phase-angles for the three pressure transducers at

approximately 10% span. The unsteady pressure waves impact the pressure side of the blade at essentially the same time. That is, the time-lag associated with propagating unsteadiness due to wakes from the nozzle guide vanes is absent in this case. Additionally, it was found that the peak level of unsteadiness occurring on the airfoil surface was directly proportional to the magnitude of the predicted steady circumferential distortion in static pressure as viewed from the blade frame of reference. Note that this is in contrast to the work of Kielb et al. [78] and Bailie et al. [79] where steady total pressure variations were taken as an indicator of blade unsteadiness in other studies where the flowfield was dominated by wake disturbances.

The results of both time-mean and steady-state predictions are plotted in Fig. 4.2. Seen from the blade frame of reference, the steady pressure field at the vane exit (approximately 25% of the vane axial chord downstream of the trailing edge) is a time-varying pressure. As such, it is amenable to Fourier analysis, and preliminary estimates of the effects of nozzle-guide-vane design changes on the blade unsteadiness, including the effect of asymmetric vane spacing, are possible. Also, optimization of the airfoil shape is possible using the steady-state design system at P&W [52], so that is another potential means of reducing unsteady forcing. However, it always remains to obtain the best possible estimate of the change in resonant stress with a full unsteady analysis of the flowfield in conjunction with structural analysis [13]. Nevertheless, this is one way that levels of unsteadiness can be controlled during the design process.
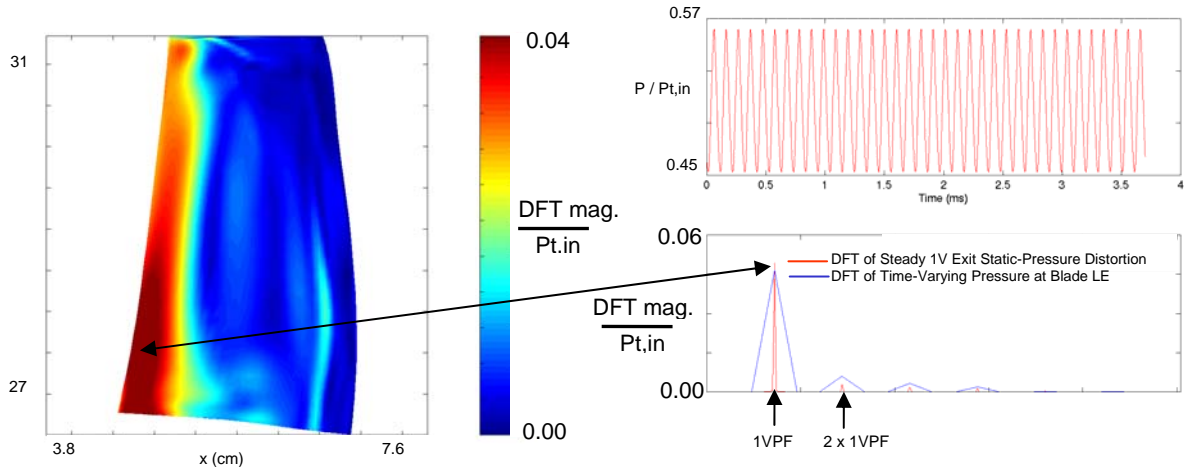

Fig. 4.2   DFT magnitude on the 1B SS (a) compares very well with the steady circumferential distortion in static pressure at the 1V exit plane at the same radius (b).

4.1   Asymmetric Vane Spacing

It is well known that asymmetric airfoil spacing can result in decreased levels of unsteady forcing at specific frequencies. An example of this is shown in Fig. 4.3. In the figure, the predicted level of unsteadiness at 1VPF on the suction side of the airfoil is shown for an asymmetric wheel composed of 1/2 wheel having a vane/blade count ratio of 3:5 and the other 1/2 wheel with a 2:3 count ratio. Also indicated is a plot of static pressure versus time corresponding to the passage of a blade around the full wheel of asymmetric vanes. In addition, plots of the same signal in the frequency domain are given. Due to the asymmetric vane spacing, the spectral peak resulting from the interaction of the blades with the vanes in the 3:5 count-ratio portion of the wheel is broader and has lower amplitude than that which would occur in the case of a full wheel of evenly spaced vanes with a 3:5 count ratio. Also,

an additional broad-banded peak occurs due to the interaction of the blades with the portion of the vane-ring having a 2:3 count ratio. The amplitude of the unsteadiness resulting from the latter segment of the vane ring is lower, however. This is because a larger number of vanes is required for the 2:3 count portion of the wheel. In consequence, a more open stagger was needed to hold the same gage area over the entire vane ring. Figure 4.4 is a comparison of the predicted DFT magnitudes on the HPT blade pressure and suction surfaces at 1VPF between the symmetric and asymmetric vane rings. The reduction in unsteadiness due to asymmetry is of order 50%. However, an asymmetric vane ring is more costly in terms of tooling and part count than a symmetric one.

3:5 vane portion of the wheel, p-p level > 0.09 Pt,in. This suggests a 1VPF DFT magnitude > 0.045 Pt,in. Asymmetry reduces that level to 0.023 Pt,in.

Spectral peaks are broader and magnitudes are smaller than suggested by time-resolved pressures due to the 3:5 and 2:3 vane/blade portions of the wheel.
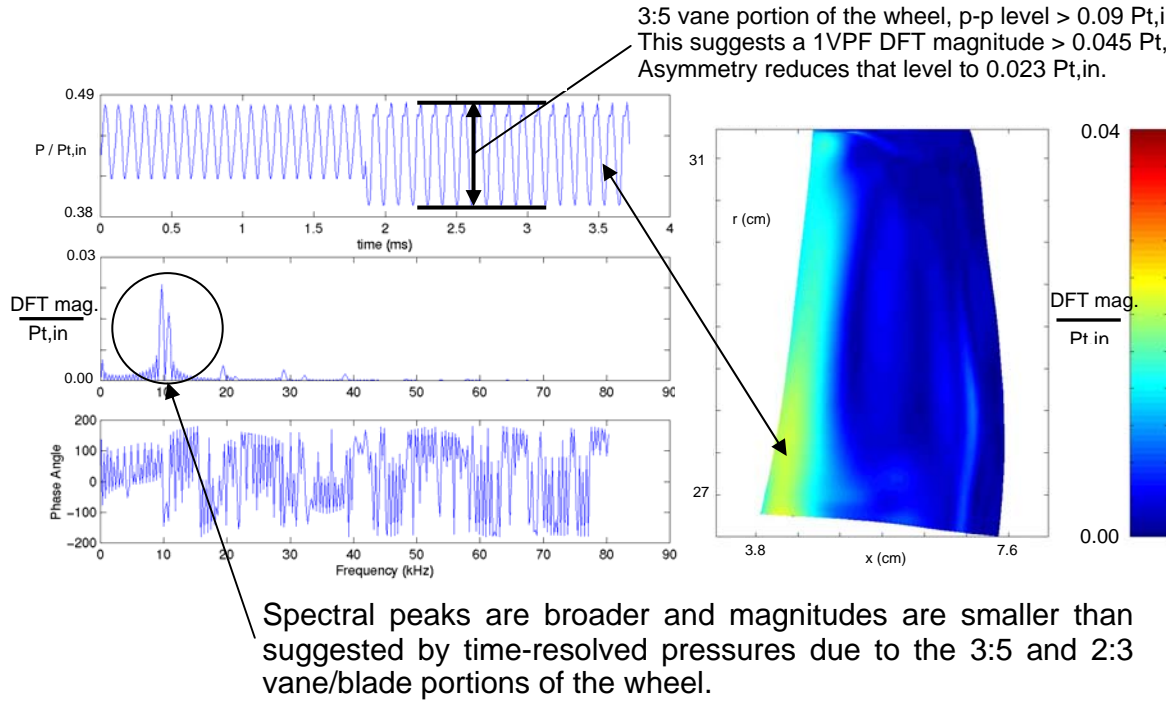
Fig. 4.3   The effect of asymmetric vane-spacing on time- and frequency-resolved predictions. Asymmetric spacing reduces DFT magnitudes over the entire 1B surface

The results of the code-validation study in the previous section were kept utmost in mind during all analyses of asymmetric vane-spacing: no airfoil scaling was used in any asymmetric analysis. Also, for each asymmetric vane ring the 3D time-resolved flowfield was solved twice, and 1B signals were concatenated in time (with appropriate phase shift) to give a "full-wheel" analysis (See Fig. 4.5). This method of analysis, which was also used for a compressor stage by Kaneko et al. [80], is somewhat less rigorous than a true full-wheel calculation, but it allowed for a significant saving in computational resources. For example, to analyze a true full-wheel with asymmetric vanes would require of order 100 Central Processing Units (CPUs), while the two-solution method required just 13 CPUs (a 3:5 model for one half of the wheel and a 2:3 model for the other). This savings meant that it was possible to investigate multiple asymmetric vane rings, and this became essential to the success of the asymmetric design.   However, the simplifications inherent in the two-step approach result in regions of discontinuity where the two solutions meet. But, this results only in wide-bandwidth, low-power unsteadiness. That is, this simplified analysis does

capture the salient features of the flowfield downstream of an asymmetric vane ring for this application.
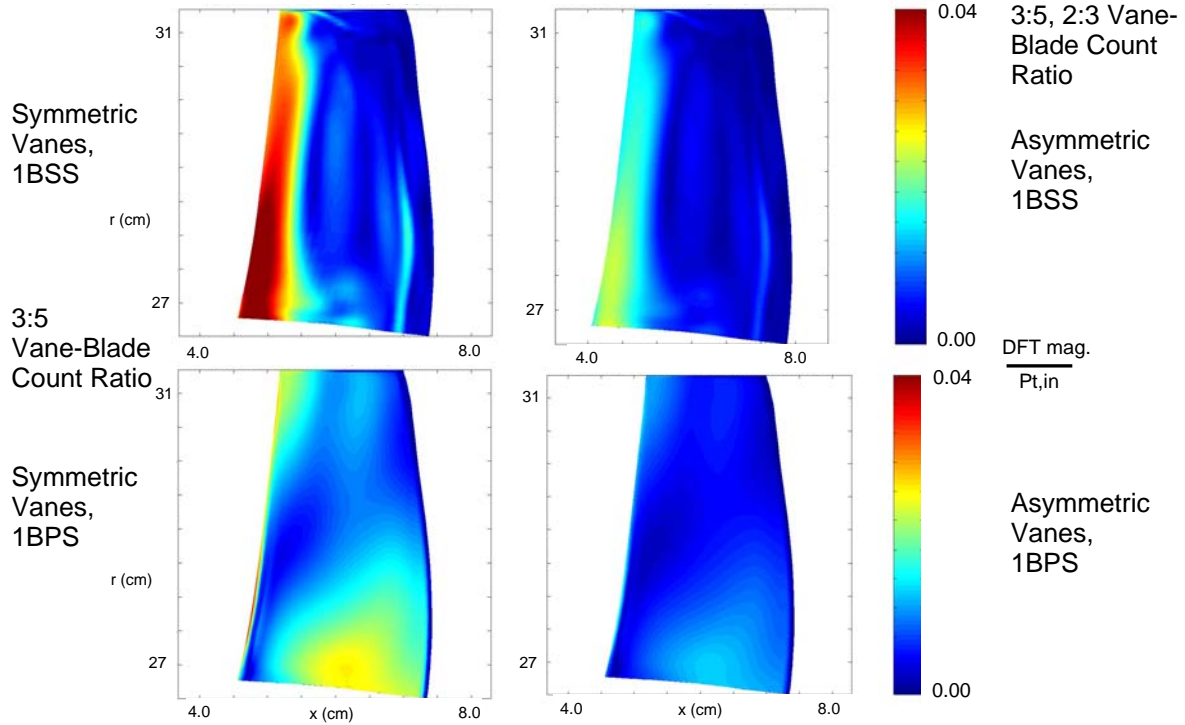

Fig. 4.4   Asymmetric vane-spacing results in a significant reduction of 1B unsteadiness levels at 1VPF. The symmetric vane-ring configuration is that denoted as "Original" in Table 4.2, while the asymmetric vanes represent "Asymmetric #1."

One way to keep the life-cycle cost of an asymmetric vane ring down would be to reduce the overall vane count. That is, it would be advantageous to remove vanes instead of adding them. However, the two-solution analysis was used to show why this does not yield a viable solution to the vibration problem. For example, if an asymmetric vane ring composed of 1/2 wheel with a 3:5 count and the other half with a 8:15 vane/blade count ratio is used, the unsteadiness due to the interaction of the blade with the 8:15 count portion of the wheel is larger than the original level of unsteadiness at the 1VPF (See Fig. 4.6). This is because fewer vanes are needed in the 8:15 count portion of the wheel, and these vanes must be staggered closed to hold the overall vane-ring throat area. In general, closing vanes tends to increase the level of circumferential static-pressure distortion, as does lowering vane count in the case of a symmetric vane ring (See, e.g. Jocker et al. [81]). Again, knowledge of the steady flowfield alone allows one to deduce the trend, but 3D time-accurate analysis is required to determine the true magnitude of the increased level of forcing.
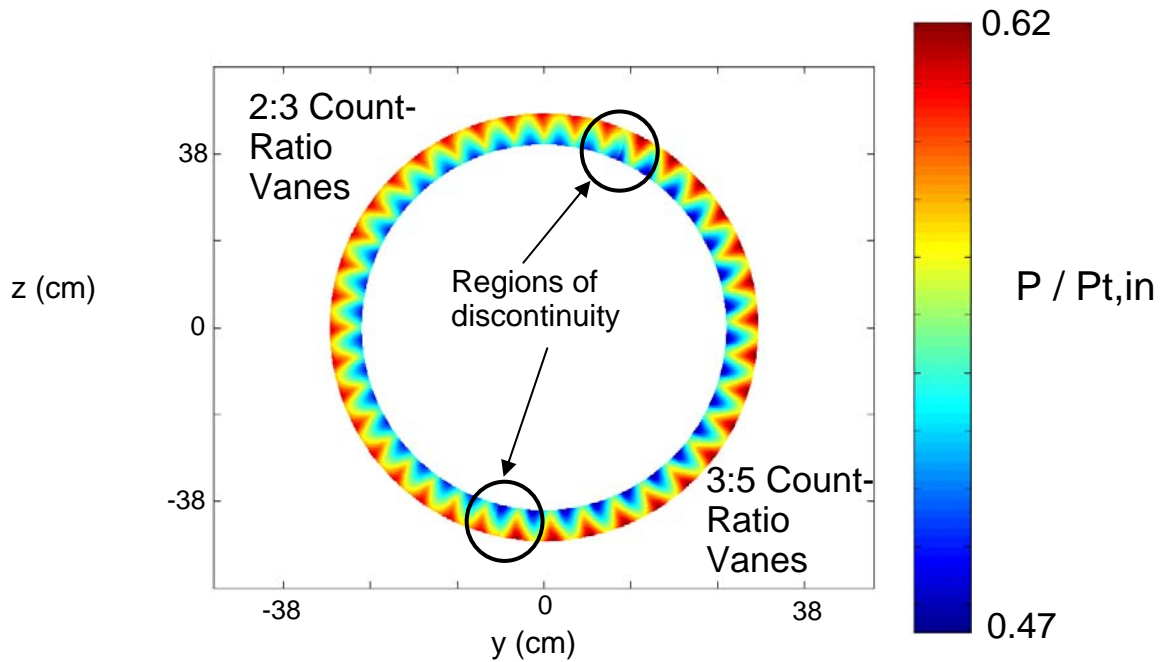
Fig. 4.5   1V exit plane static-pressure contours for an asymmetric vane-ring.

4.2   Vane Re-Design Using Optimization Techniques

Optimization of the 1V suction surface was performed using commercially available software in conjunction with P&W developed CFD tools as described by Staubach [52]. Other optimization studies designed to limit resonant stress also appear in the literature (See, e.g. Li et al. [82]). Here, a single row, 3D, steady, RANS analysis was performed with a relatively coarse grid (See Table 4.1), and three radial airfoil sections (root, mean and tip) were independently optimized. These design sections were periodically combined and then re-optimized. This method offered significant speed up in obtaining an optimum design. Each section was re-designed by perturbing the existing vane surface in conjunction with a gradient-search optimization algorithm called the Modified Method of Feasible Directions. This particular algorithm features a direct method of dealing with constraints (Vanderplaat [83]). The optimization goal was to minimize the circumferential static-pressure distortion 25% of the vane axial chord downstream of the vane trailing edge by adjusting the local suction side curvature of the 1V.
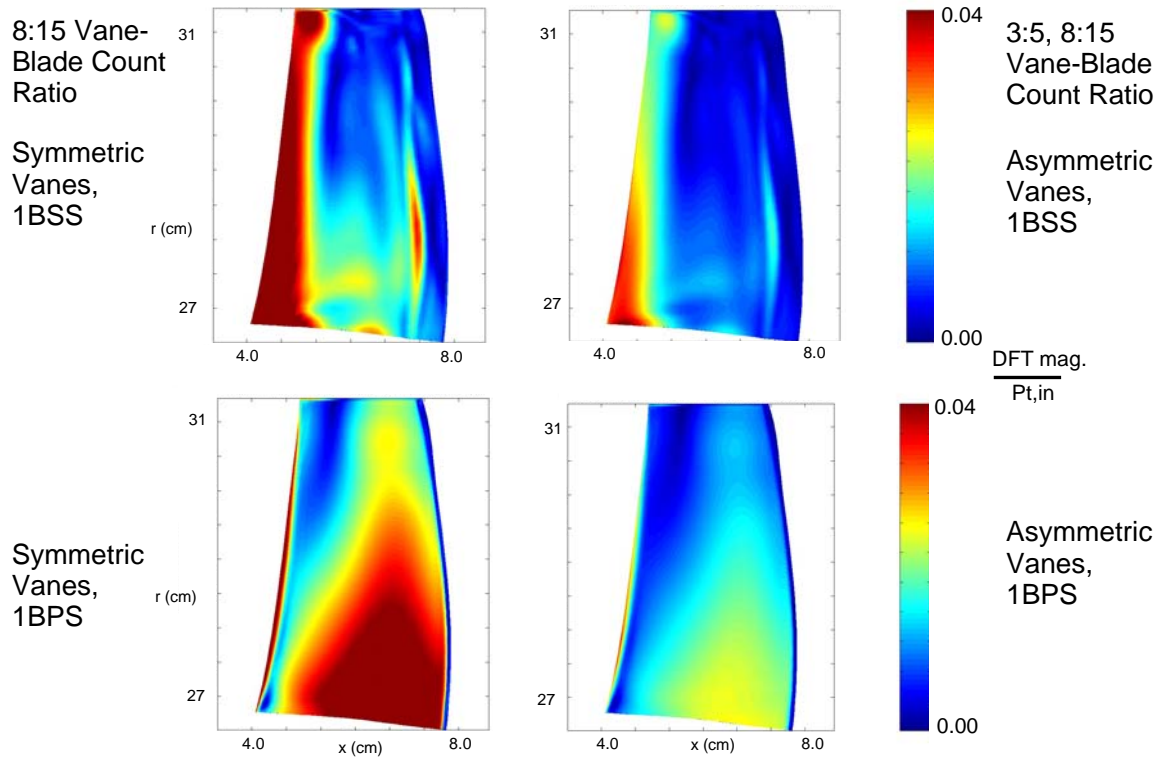
Fig. 4.6   An asymmetric vane ring with 3:5 and 8:15 ratios was also investigated. This "Asymmetric #2" configuration resulted in increased levels of predicted unsteadiness at 1VPF.

Table 4.1: Details of CFD models used for re-design and analysis.

	1V	1B
Airfoils Modeled in Each Row		
Symmetric Design	3	5
Asymmetric Design #1		
1/2 Wheel	3	5
1/2 Wheel	2	3
Asymmetric Design #2		
1/2 Wheel	3	5
1/2 Wheel	8	15

Axial x Radial x Circumferential Grid Counts :

Within Optimization Algorithm	81x33x33	
During Time-Accurate Analysis	89x49x57	145x49x57 *

* Each blade also had a 57x16x16 Tip-Clearance Grid

At various points in the optimization process, the algorithm was halted and more rigorous checks were performed on the vane-blade interaction. These included Fourier analysis of the exit static-pressure field and, in some cases, full 3D unsteady analysis and resonant stress-prediction with Pratt & Whitney aeromechanics analysis tools (See Hilbert et al. [13]). Throughout all the analysis, an excellent correlation was found to hold between the level of steady circumferential static-pressure distortion and the peak level of unsteadiness on the blade as illustrated in Fig. 4.2. It must be stated, however, that the peak-to-peak level of circumferential distortion is not the most critical piece of information. Most important are the magnitude and phase of the discrete Fourier transform at the frequency of interest (in this case 1VPF) and their distribution around the blade surface. For this reason, the more rigorous checks on the vane flowfield were performed at intervals throughout the analysis.

The effects of the optimized vane suction side on the predicted blade unsteady pressures are illustrated in Fig. 4.7 and Fig. 4.8. For the first-vane passing frequency (1VPF) plots in Fig. 4.7, it can be seen that the optimized vane results in a substantial reduction in the discrete Fourier-transform magnitude over the entire blade surface, and this in turn produces a reduction in predicted resonant stress. However, there is an increase in the level of unsteadiness for the first harmonic of the vane-passing frequency (2x1VPF), as shown in Fig. 4.8. Fortunately, there were no vibratory stress problems due to 2x1VPF crossings, and the increases in unsteadiness were at locations where little blade motion would be expected. So, although the unsteadiness increased at 2x1VPF, predicted levels of resonant stress were acceptable for all twice vane-passing crossings. Again, this points to the need for more rigorous analyses during the optimization process. If one optimizes the vane by reducing peak-to-peak levels of circumferential distortion only and did not consider crossings due to frequencies other than that of immediate interest, it is possible to have a very serious design escape. That is, when one uses an optimization process to improve a design, it is as important to keep the overall health of the design in mind as it is to solve the problem of most pressing interest.

4.3   Design Decisions and Solution Assessment

For each vane-ring configuration considered as a serious candidate to reduce the first-torsion-mode resonant stress, a complete time-accurate analysis was completed to determine vibratory-stress estimates as well as amplitudes of unsteady forcing. The results are summarized in Table 4.2. It can be seen that both the vanes with the re-designed suction sides and the asymmetric vane-ring could be used to reduce the first-torsion stress by approximately 50%. However, the optimized vanes allowed for a 51% stress reduction with very minor modifications to the profile of the vanes. Again, the part count and tooling of a prototype asymmetric vane ring are both larger than the modified-vane design.
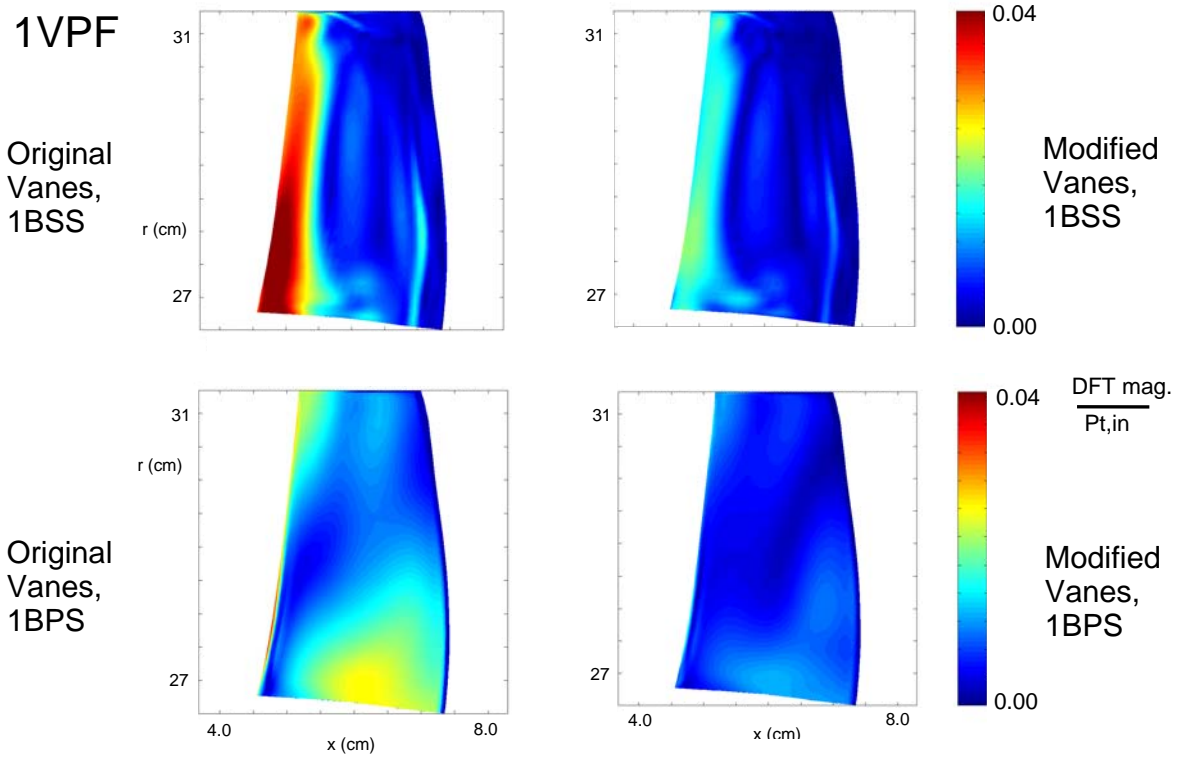
Fig. 4.7   1V re-design resulted in significantly lower unsteadiness at 1VPF.
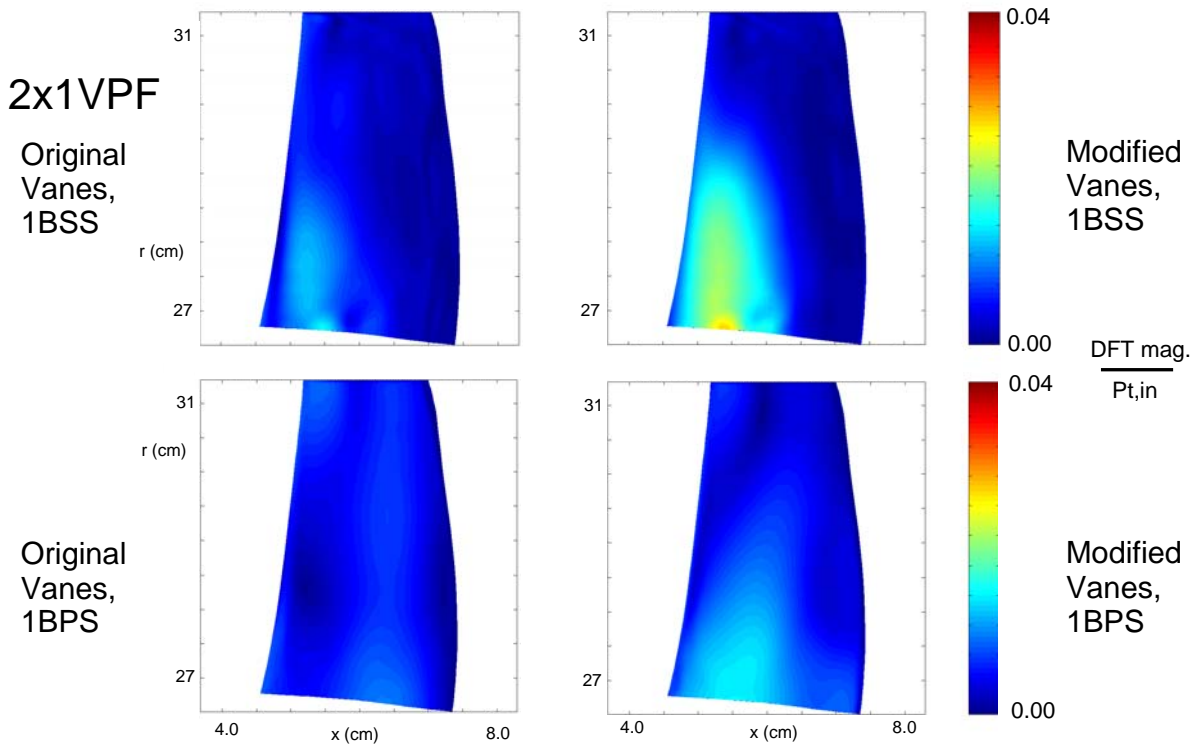

Fig. 4.8   The 1V re-design resulted in increased 1B unsteadiness at 2 x 1VPF.

Table 4.2: Summary of predicted levels of resonant-stress for various vane-ring configurations.

Vane-Ring Configuration	Stress Driver	First-Torsion Resonant Stress, MPa (ksi)	Percent Difference
Original (3:5)	1VPF	103 (14.9)	N/A
Asymmetric #1			
3:5 Portion	1VPF	55 (8.0)	-46
2:3 Portion	1VPF	26 (3.8)	-75
Asymmetric #2			
3:5 Portion	1VPF	55 (8.0)	-46
8:15 Portion	1VPF	128 (18.6)	24
Modified Suction			
Side (3:5)	1VPF	51 (7.4)	-51

Subsequently, resonant stress measurements were made in prototype engines. One engine contained a vane ring composed entirely of optimized vanes that were created using EDM tools to alter the suction sides of vane castings of the original shape that already existed. Thus the additional cost of the prototype engine was kept quite low.   Prior to the test, the average profile shape of 70% of the vanes was measured, and the resulting vane-geometry was analyzed with the Pratt & Whitney aeromechanics analysis-system as described by Hilbert et al. [13]. For these vanes, the predicted decrease in blade resonant stress due to the design change was 42% as compared to the 51% reduction predicted for the vanes that had the intended modification. Measurements in the prototype engine confirmed a reduction in stress of 36%. Then, in another demonstrator engine, a vane ring was composed of one-half wheel of optimized vanes and one-half wheel as analyzed in asymmetric configuration #1. An additional reduction in blade resonant stress (as expected from Table 4.2) due to the use of vane asymmetry in conjunction with the modified vanes was confirmed.

4.4   Conclusions

Modern aerodynamic design and analysis tools were used successfully to predict and to control the level of unsteady forcing in a gas turbine engine during the design cycle. In this study, the maximum level of unsteady forcing that occurred on the blade surface due to potential-field interaction with the upstream vane row scaled directly with the peak-to-peak amplitude of the predicted steady-state static pressure variation in the circumferential direction at the vane exit.   This knowledge, combined with accurate benchmarking of predicted levels of unsteady forcing functions in a high-pressure turbine stage enabled analysts to reduce resonant stress levels during the design cycle. It was shown that either appropriate vane asymmetry or modifications of the vane suction side to reduce levels of peak-to-peak static pressure distortion resulted in viable design solutions to reduce resonant stress in the first torsion mode. Of the two design alternatives found, modification of the vane suction side was most attractive because it resulted in minimal changes to the original vane-ring geometry, and testing in development engines confirmed the predicted benefits of the design changes.

5. Summary

In this lecture, a successful example of the reduction of unsteady forcing via appropriate aerodynamic design changes made during the development of a transonic turbine stage was presented. It was argued that aerodynamic designers must gain confidence in their predictions of time-varying loads on rotating airfoils prior to any attempt to mitigate unsteady interaction between airfoils rows. This confidence is achievable through rigorous checks on the convergence of simulations coupled with judicious post-processing of predicted flowfields with respect to the requirements and limitations of resonant-stress evaluation systems. Further, the usefulness of proactive validation and verification exercises targeted at design-level predictions of airfoil unsteady pressures in relevant physical environments was demonstrated. It was shown that it is possible to leverage the lessons learned from such code validation studies directly in the development of new turbomachines. By performing the most rigorous unsteady analyses possible given available time and computational resources several possible design solutions to a resonant-stress problem were evaluated. Then, simple and effective means for mitigating unsteady interaction in a single-stage high pressure turbine were implemented and verified in demonstrator-engine tests.

6. References

[1] Tyler, J. M. and Sofrin, T. G., 1970, "Axial Flow Compressor Noise Studies," SAE Transactions, Vol. 70, pp. 309-332.

[2] Rangwalla, A. A. and Rai, M. M., 1993, "A Numerical Analysis of Tonal Acoustics in Rotor-Stator Interactions," Journal of Fluids and Structures, Vol. 7, pp. 611-637.

[3] Dring, R. P., Joslyn, H. D., Hardin, L. W., and Wagner, J. H., 1982, "Turbine Rotor-Stator Interaction , ASME Journal of Engineering for Power," Vol. 104, pp. 729-742.

[4] Dunn, M. G. and Haldeman, C. W., Jr., 1995, "Phase-Resolved Surface Pressure and Heat-Transfer Measurements on the Blade of a Two-Stage Turbine," ASME Journal of Fluids Engineering, Vol. 117, pp. 653-658.

[5] Rai, M. M., 1987, "Navier-Stokes Simulations of Rotor-Stator Interaction Using Patched and Overlaid Grids," AIAA Journal of Propulsion and Power, Vol. 3, pp. 387-396.

[6] Giles, M. B., 1990, "Stator/Rotor Interaction in a Transonic Turbine," AIAA Journal of Propulsion and Power, Vol. 6, pp. 621-627.

[7] Greitzer, E. M., Tan, C. S., Wisler, D. C., Adamczyk, J. J., and Strazisar, A. J., 1994. Unsteady Flows in Turbomachines: Where's the Beef?," Unsteady Flows in Aeropropulsion, ASME AD-Vol. 40, pp. 1-11.

[8] Sharma, O. P., Pickett, G.F., and Ni, R.H., 1992, "Assessment of Unsteady Flows in Turbines," ASME Journal of Turbomachinery, Vol. 114, pp. 79-90.

[9] Paniagua, G. and Denos, R., 2007, "Unsteadiness in HP Turbines," in Advances in Turbomachinery Aero-Thermo-Mechanical Design Analysis, VKI Lecture Series 2007-02.

[10] Dunn, M. G., 2001, "Convective Heat Transfer and Aerodynamics in Axial Flow Turbines," ASME Journal of Turbomachinery, Vol. 123, pp. 637-686.

[11] Adamczyk, J. J., 2000, "Aerodynamic Analysis of Multi-Stage Turbomachinery Flows in Support of Aerodynamic Design," ASME Journal of Turbomachinery, Vol. 122, pp. 189-217.

[12] Ni, R.H., "Advanced Modeling Techniques for New Commercial Engines," 1999, XIV ISOABE Conference, Florence, Italy, 5-10 September.

[13] Hilbert, G. R., Ni, R. H., and Takahashi, R. K., 1997, "Forced-Response Prediction of Gas Turbine Rotor Blades," Analysis and Design Issues for Modern Aerospace Vehicles, Proceedings of the Symposia, ASME International Mechanical Engineering Congress and Exposition, Dallas, TX, 16-21 Nov., pp. 491-498.

[14] Green, J. S. and Marshall, J. G., 1999, "Forced Response Prediction within the Design Cycle," IMechE Conference Transactions 1999-1A, pp. 377-391.

[15] Chiang, H. D. and Kielb, R. E., 1993, "An Analysis System for Blade Forced Response," ASME Journal of Turbomachinery, Vol. 115, pp. 762-770

[16] Seinturier, E., Lombard, J-P., Dumas, M., Dupont, C., Sharma, V., Dupeux, J., 2004, "Forced-Response Methodology for the Design of HP Compressors Bladed Disks," ASME Paper No. GT2004-53372.

[17] Montgomery, M., Tartibi, M., Eulitz, F., and Schmitt, S., 2005, "Application of Unsteady Aerodynamics and Aeroelasticity in Heavy Duty Gas Turbines," ASME Paper No. GT2005-68813.

[18] Filsinger, D., Frank, Ch., and Schafer, O., 2005, "Practical Use of Unsteady CFD and FEM Forced Response Calculation in the Design of Axial Turbocharger Turbines," ASME Paper No. GT2005-68439.

[19]   Sipatov, A. M., Gladisheva, N. V., Avgustinovich, V. G., and Povishev, I. A., 2007, "Tools for Estimating Resonant Stresses in Turbine Blades," ASME Paper No. GT2007-27196.

[20]   Jones, T. V., Schultz, D. L., and Henley, A. D., 1973, "On the Flow in an Isentropic Light Piston Tunnel," ARC Report No. 34217, U.K.

[21]   Dunn, M. G., Moller, J. C., and Steele, R. C., 1989, "Operating Point Verification for a Large Shock Tunnel Test Facility," Calspan Report No. WRDC-TR-2027.

[22]   Rao, K. V., Delaney, R.A., and Dunn, M.G., 1994, "Vane-Blade Interaction in a Transonic Turbine, Part 1: Aerodynamics," ASME Journal of Propulsion and Power, Vol. 10, No. 3, pp. 305-311.

[23]   Busby, J. A., Davis, R. L., Dorney, D. J., Dunn, M. G., Haldeman, C. W., Jr., Abhari, R. S., Venable, B. L., and Delaney, R. A., 1998. Influence of Vane-Blade Spacing on Transonic Turbine Stage Aerodynamics, Part II: Time-Resolved Data and Analysis, ASME Paper No. 98-GT-482.

[24]   Hilditch, M. A., Smith, G. C., and Singh, U. K., 1998, "Unsteady Flow in a Single Stage Turbine," ASME Paper No. 98-GT-531.

[25]   Haldeman, C. W., Dunn, M. G., Abhari, R. S., Johnson, P. D., and Montesdeoca, X. A., 2000, "Experimental and Computational Investigation of the Time-Averaged and Time-Resolved Pressure Loading on a Vaneless Counter-Rotating Turbine," ASME Paper No. 2000-GT-0445.

[26]   Kost, F., Hummel, F., and Tiedemann, M., 2000, "Investigation of the Unsteady Rotor Flow in a Single-Stage HP Turbine Stage," ASME Paper No. 2000-GT-0432.

[27]   Laumert, B., Martensson, H, and Fransson, T. H., 2002, "Investigation of Unsteady Aerodynamic Blade Excitation Mechanisms in a Transonic Turbine Stages," ASME Paper No. GT2002-30450.

[28]   Bakhle, M. A., Liu, J. S., Panovsky, J., Keith, T. G., and Mehmed, O., 2002, "Calculation and Correlation of the Unsteady Flowfield in a High Pressure Turbine," ASME Paper No. GT2002-30322.

[29]   Kielb, J. J., Abhari, R. S., and Dunn, M. G., 2001, "Experimental and Numerical Study of Forced Response in a Full-Scale Rotating Turbine," ASME Paper No. 2001-GT-0263.

[30]   Hennings, H. and Elliot, R., 2002, "Forced Response Experiments in a High Pressure Turbine Stage," ASME Paper No. GT2002-30453.

[31]   Kielb, J. J. and Abhari, R. S., 2001, "Experimental Study of Aerodynamic and Structural Damping in a Full-Scale Rotating Turbine," ASME Paper No. 2001-GT-0263.

[32]   Jennions, I. K. and Adamczyk, J. J., 1997, "Evaluation of the Interaction Losses in a Transonic Turbine HP Rotor / LP Vane Configuration," ASME Journal of Turbomachinery, Vol. 119, pp. 68-75.

[33]   Ni, R. H., 1982, "A Multiple-Grid Scheme for Solving the Euler Equations," AIAA Journal, Vol. 20, No. 11, pp. 1565-1571.

[34]   Ni, R. H. and Bogoian, J. C., 1989, "Prediction of 3-D Multistage Turbine Flow Field Using a Multiple-Grid Euler Solver," AIAA Paper No. 89-0203.

[35]   Davis, R. L., Shang, T., Buteau, J., and Ni, R. H., 1996, "Prediction of 3-D Unsteady Flow in Multi-Stage Turbomachinery Using an Implicit Dual Time-Step Approach," AIAA Paper No. 96-2565.

[36] Weaver, M. M., Manwaring, S. R., Abhari, R. S., Dunn, M. G., Salay, M. J., Frey, K. K., and Heidegger, N., 2000, "Forcing Function Measurements and Predictions of a Transonic Vaneless Counter-Rotating Turbine," ASME Paper No. 2000-GT-0375.

[37] Huber, F., Johnson, P. D., Sharma, O. P., Staubach, J. B., and Gaddis, S. W., 1996, "Performance Improvement Through Indexing of Turbine Airfoils: Part 1- Experimental Investigation," ASME Journal of Turbomachinery, Vol. 118, pp. 630-635.

[38] Griffin, L. M., Huber, F. W., and Sharma, O. P., "Performance Improvement Through Indexing of Turbine Airfoils: Part 2- Numerical Simulation," ASME Journal of Turbomachinery, Vol. 118, pp. 636-642.

[39] Dorney, D. J., and Sharma, O. P., 1996, "A Study of Turbine Performance Increases Through Clocking," AIAA Paper No. 96-2816.

[40] Haldeman, C. W., Dunn, M. G., Barter, J. W., Green, B. R., and Bergholz, R. F., 2005, "Experimental Investigation of Vane Clocking in a One and 1/2 Stage High Pressure Turbine, ASME Journal of Turbomachinery, Vol. 127, pp. 512-521 (Also ASME Paper No. GT2004-5347).

[41] Shang, T. and Epstein, A. H., 1997, "Analysis of Hot Streak Effects on Turbine Rotor Heat Load," ASME Journal of Turbomachinery, Vol. 119, No. 3, pp. 544-553..

[42] Takahashi, R. K., Ni, R. H., Sharma, O. P., and Staubach, J. B., 1996, "Effects of Hot Streak Indexing in a 1-1/2 Stage Turbine," AIAA Paper No. 96-2796.

[43] Dorney, D. J., and Gundy-Burlet, K., 2000, "Hot-Streak Clocking Effects in a 1-1/2 Stage Turbine," AIAA Journal of Propulsion and Power, Vol. 12, No. 3, pp. 619-620.

[44] He, L., Menshikova, V., and Haller, B. R., "Influence of Hot Streak Circumferential Length-Scale in a Transonic Turbine Stage," ASME Paper No. GT2004-53370.

[45] Munk, M. and Prim, R., 1947, "On the Multiplicity of Steady Gas Flows Having the Same Streamline Pattern," Proceedings of the National Academy of Sciences, Vol. 33, pp. 137-141.

[46] Roache, P. J., 1998, Verification and Validation in Computational Science and Engineering, Hermosa Publishers, Albuquerque, NM, USA.

[47] Gokaltun, S., Skudarnov, P. V., and Lin, C-X., 2005, "Verification and Validation of CFD Simulation of Pulsating Laminar Flow in a Straight Pipe," AIAA Paper No. 2005-4863.

[48] Guide for the Verification and Validation of Computational Fluid Dynamics Simulations, AIAA Policy Paper G-077-1998, AIAA, Reston, VA, USA.

[49] Freitas, C. J., 1993, "Editorial Policy Statement on the Control of Numerical Accuracy," ASME *Journal of Fluids Engineering*, Vol. 115, No. 2, pp. 339.

[50] Laumert, B., Martensson, H, and Fransson, T. H., 2002, "Investigation of Unsteady Aerodynamic Blade Excitation Mechanisms in a Transonic Turbine Stage, Part I: Phenomenological Identification and Classification," ASME Journal of Turbomachinery, Vol. 124, pp. 410-418 (Also ASME Paper No. 2001-GT-0258).

[51] Ahmed, M. H. and Barber, T. J., 2005, "Fast Fourier Transform Convergence Criterion for Numerical Simulations of Periodic Fluid Flows," AIAA Journal, Vol. 43, No. 5, pp. 1042-1052.

[52] Staubach, J. B., 2003, "Multidisciplinary Design Optimization, MDO, the Next Frontier of CAD/CAE in the Design of Aircraft Propulsion Systems," AIAA Paper No. 2003-2803.

[53] Shahpar, S. and Lapworth, L., 2003, "PADRAM: Parametric Design and Rapid Meshing for Turbomachinery Optimization," ASME Paper No. GT2003-38698.

[54]   Shahpar, S., Giacche, D., and Lapworth, L., 2003, "Multi-Objective Design and Optimization of Bypass Outlet-Guide Vanes," ASME Paper No. GT2003-38700.

[55]   Ifeachor, E. C. and Jervis, B. W., 1996, Digital Signal Processing, Addison-Wesley, New York.

[56]   Signal Processing Toolbox User's Guide, Version 5, 2000, The Mathworks, Natick, MA.

[57]   Jocker, M., and Fransson, T. H., 2002, "Mode Shape Sensitivity of the High Pressure Turbine Rotor Excitation Due to Upstream Stators," ASME Paper No. GT2002-30452.

[58]   Klir, G.J., St. Clair, U.H., and Yuan, B., 1997, Fuzzy Set Theory: Foundations and Applications, Prentice Hall PTR, Upper Saddle River, NJ.

[59]   Clark, J.P. and Yuan, B., 1998, "Using Fuzzy Logic to Detect Turbulent/Non-Turbulent Interfaces in an Intermittent Flow," Intelligent Automation and Control, Vol. 6, pp. 113-118, TSI Press, Albuquerque, NM

[60]   Zimmermann, H. J. 1990, Fuzzy Set Theory and Its Applications, Second Edition, Kluwer, Boston, MA.

[61]   Klir, G. J. and Yuan, B., 1995, Fuzzy Sets and Fuzzy Logic: Theory and Applications, Prentice Hall PTR, Upper Saddle River, NJ.

[62]   Johnson, P. D., 2005, "Consortium Turbine Research Rig, Aerothermal and Mechanical Design," AFRL Technical Report AFRL-PR-WP-TR-2005-2157.

[63]   Dorney, D. J. and Davis, R. L., 1992, "Navier-Stokes Analysis of Turbine Blade Heat Transfer and Performance," ASME Journal of Turbomachinery, Vol. 114, pp. 795-806.

[64]   Rai, M. M. and Madavan, N. K., 1990, "Multi-Airfoil Navier-Stokes Simulations of Turbine Rotor-Stator Interaction," ASME Journal of Turbomachinery, Vol. 112, pp. 377-384.

[65]   Polanka, M.D., Hoying, D.A., Meininger, M., and MacArthur, C.D., 2003, "Turbine Tip and BOAS Heat Transfer and Loading, Part A: Parameter Effects Including Reynolds Number, Pressure Ratio and Gas to Metal Temperature Ratio", ASME Journal of Turbomachinery, Vol. 125, pp. 97-106.

[66]   Clark, J. P., Polanka, M. D., Meininger, M., and Praisner, T. J., 2006, "Validation of Heat-Flux Predictions on the Outer Air Seal of a Transonic Turbine Blade," ASME Journal of Turbomachinery, Vol. 128, pp. 589-595.

[67]   Kielb, R. E., Barter, J. W., Thomas, J. P., and Hall, K. C., 2003, "Blade Excitation by Aerodynamic Instabilities – A Compressor Blade Study," ASME Paper No. GT2003-38634.

[68]   Sanders, A. J., 2005, "Non-Synchronous Vibration (NSV) Due to a Flow-Induced Aerodynamic Instability in a Composite Fan Stator," ASME Journal of Turbomachinery, Vol. 127, pp. 412-421 (Also ASME Paper No. GT2004-53492).

[69]   Doorly, D. J. and Oldfield, M. L. G., 1985, "Simulation of the Effects of Shock Wave Passing on a Turbine Rotor Blade," ASME Journal of Engineering for Gas Turbines and Power, Vol. 107, pp. 998-1006.

[70]   Smith, M. C., and Kuethe, A. M., 1966, "Effects of Turbulence on Laminar Skin Friction and Heat Transfer," Physics of Fluids, Vol. 9, No. 12, pp. 2337-2344.

[71]   Baldwin, B. S. and Lomax, H., 1978, "Thin-Layer Assumptions and Algebraic Model for Separated Flow," AIAA Paper No. 78-0257.

[72]   Lax, P. D., and Wendroff, B., 1964, "Difference Schemes for Hyperbolic Equations with High Order Accuracy," Communications on Pure and Applied Mechanics, Vol. 17, pp. 381-398.

[73] Dunham, J. and Meauze, G., 1998, "An AGARD Working Group Study of 3D Navier-Stokes Codes Applied to Single Turbomachinery Blade Rows," ASME Paper No. 98-GT-50.

[74] Chen, J. P. and Briley, W. R., "A Parallel Flow Solver for Unsteady Multiple Blade Row Turbomachinery Simulations," ASME Paper No. 2001-GT-0348.

[75] Davis, R. L., Yao, J., Clark, J. P., Stetson, G. M., Alonso, J. J., Jameson, A., Haldeman, C. W., Jr., and Dunn, M. G., 2004, "Unsteady Interaction Between a Transonic Turbine Stage and Downstream Components," International Journal of Rotating Machinery, Vol. 10, No. 6, pp. 495-506.

[76] Breard, C., Green, J. S., Vahdati, M., and Imregun, M., 2000, "A Resonance Tracking Algorithm for the Prediction of Turbine Forced Response with Friction Dampers," ASME Paper No. 2000-GT-0372.

[77] Green, J. S. and Fransson, T. H., 2006, "Scaling of Turbine Blade Unsteady Pressures for Rapid Forced Response Assessment," ASME Paper No. GT2006-90613.

[78] Kielb, J., Weber, K., and Crook, B., 2007, "Innovative Design of a Robust Turbine Stage Using Flow Analysis and Subcomponent Rig Testing with Rapid Prototypes," ASME Paper No. GT2007-28256.

[79] Bailie, S. T., Ng, W. F., and Copenhaver, W. W., 2004, "Experimental Reduction of Transonic Fan Forced Response by IGV Flow Control," ASME Paper No. GT2004-53975.

[80] Kaneko, Y., Mori, K., and Okui, H., 2004, "Study of the Effect of Asymmetric Vane Spacing on Vibratory Stress of a Blade," ASME Paper No. GT2004-53023.

[81] Jocker, M., Hillion, F. X., Fransson, T. H., and Wahlen, U., 2002, "Numerical Unsteady Flow Analysis of a Turbine Stage with Extremely Large Blade Loads," ASME Journal of Turbomachinery, Vol. 124, pp. 429-438 (Also ASME Paper No. 2001-GT-0260).

[82] Li, H-D., He, L., Li, Y. S., and Wells, R., 2006, "Blading Aerodynamics Design Optimization with Mechanical and Aeromechanical Constraints," ASME Paper No. GT2006-90503.

[83] Vanderplaat, G. N., 1984, Numerical Optimization Techniques for Engineering Design: With Applications, McGraw-Hill, New York.

[84] Clark, J. P., and Grover, E. A., 2007, "Assessing Convergence in Predictions of Periodic-Unsteady Flowfields," ASME Journal of Turbomachinery, Vol. 129, pp. 740-749.

[85] Clark, J.P., Stetson, G.M., Magge, S.S., Dunn, M.G., and Haldeman, C.W., 2000, "The Effect of Airfoil Scaling on the Unsteady Aerodynamics of a 1 and 1/2 Stage Transonic Turbine and a Comparison with Experimental Results", ASME Paper No. 2000-GT-446.

[86] Clark, J. P., Aggarwala, A. S., Velonis, M. A., Magge, S. S., and Price, F. R., 2002, "Using CFD to Reduce Resonant Stresses on a Single-Stage, High-Pressure Turbine Blade," ASME Paper No.GT2002-30320.

Nomenclature

<u>Latin</u>

A	DFT magnitude
b_x	airfoil axial chord (cm)
CCF	Cross-correlation coefficient
DFT	Discrete Fourier Transform
E	Engine order = frequency / (rpm / 60)
f	Membership grade in a fuzzy set
k	Integer multiple of sampling frequency
L	Number of lags
M	Mach number
n_{af}	number of airfoils in a given row
N	wheel speed (rpm)
N	Number of samples per periodic cycle
n	Integer multiple of sampling interval
P	Fourier component of static pressure signal
Pt,in	Inlet total pressure (M Pa)
p	Static pressure (M Pa)
PS	pressure side
PSD	Power spectral density
r	radial distance (cm, in)
Re	Reynolds number based on axial chord
SS	suction side
T_t	Total temperature (K)
Tu	turbulence intensity (%)
U	rotor tangential velocity (m/s)
x	axial distance (cm, in)
y^+	non-dimensional distance (law-of-the-wall variable)
1B	first blade
1V	first vane
1VPF	first vane passing-frequency (fundamental) = (n_{af} N) / 60
2V	second vane

<u>Greek</u>

Δf	Spectral resolution (Hz) of a signal = 1 / (N Δt)
Δt	Sampling rate, temporal resolution of a signal (s)
Φ	DFT phase angle (radians, degrees)
ω	Circular frequency (radians / s)

<u>Subscripts / Superscript</u>

A	Fuzzy set for convergence of DFT amplitude
C	Fuzzy set for overall convergence
M	Fuzzy set for time-mean convergence
P	Fuzzy set for fraction of overall signal power
S	Fuzzy set for convergence of overall signal shape
Φ	Fuzzy set for convergence of DFT phase angle
'	Fluctuating component